

# Energized Oxygen in the Magnetotail: Onset and Evolution of Magnetic Reconnection

Don E George<sup>1</sup> and Jorg-Micha Jahn<sup>1</sup>

<sup>1</sup>Southwest Research Institute

November 26, 2022

## Abstract

Oxygen ions are a major constituent of magnetospheric plasma, yet the role of oxygen in processes such as magnetic reconnection is poorly understood. Observations show that significant energized  $O^+$  can be present in a magnetotail current sheet. A population of thermal  $O^+$  only has a minor effect on magnetic reconnection. Despite this, published studies have so far only concentrated on the role of the low-energy thermal  $O^+$ . We present a study of magnetic reconnection in a thinning current sheet with energized  $O^+$  present. Well-established, three-species, 2.5D Particle-In-Cell (PIC) kinetic simulations are used. Simulations of thermal  $H^+$  and thermal  $O^+$  validate our setup. We energize a thermal background  $O^+$  based on published measurements. We apply a range of energization to the background  $O^+$ . We discuss the effects of energized  $O^+$  on current sheet thinning and the onset and evolution of magnetic reconnection. Energized  $O^+$  has a major impact on the onset and evolution of magnetic reconnection. Energized  $O^+$  causes a two-regime onset response in a thinning current sheet. As energization increases in the lower-regime, reconnection develops at a single primary  $\{X\}$ -line, increases time-to-onset, and suppresses the rate of evolution. As energization continues to increase in the higher-regimes, reconnection develops at multiple  $\{X\}$ -lines, forming a stochastic plasmoid chain; decreases time-to-onset; and enhances evolution via a plasmoid instability. Energized  $O^+$  drives a depletion of the background  $H^+$  around the current sheet. As energization increases, the thinning begins to slow and eventually reverses, leading to disruption of the current sheet via a plasmoid instability.

# Energized Oxygen in the Magnetotail: Onset and Evolution of Magnetic Reconnection

Don E George<sup>1,2</sup>, Jörg-Micha Jahn<sup>1,2</sup>

<sup>1</sup>Space Science and Engineering, Southwest Research Institute, San Antonio, Texas, USA.

<sup>2</sup>Department of Physics and Astronomy, University of Texas at San Antonio, San Antonio, Texas, USA

## Key Points:

- Energized  $O^+$  has a major impact on the onset and evolution of magnetic reconnection.
- The presence of energized  $O^+$  causes a two-regime onset response in a thinning current sheet.
- At lower energization,  $O^+$  increases time-to-onset and suppresses the rate of evolution; at higher energization, the opposite occurs.

**Abstract**

Oxygen ions are a major constituent of magnetospheric plasma, yet the role of oxygen in processes such as magnetic reconnection continues to be poorly understood. Observations show that significant amounts of energized  $O^+$  can be present in a magnetotail current sheet. A population of thermal  $O^+$  only has a minor effect on magnetic reconnection. Despite this, published studies have so far only concentrated on the role of the low-energy thermal  $O^+$ .

We present a study of magnetic reconnection in a thinning current sheet with energized  $O^+$  present. Well-established, three-species, 2.5D Particle-In-Cell (PIC) kinetic simulations are used. Simulations of thermal  $H^+$  and thermal  $O^+$  validate our setup against published results. We then energize a thermal background  $O^+$  based on published in-situ measurements. A range of energization is applied to the background  $O^+$ . We discuss the effects of energized  $O^+$  on current sheet thinning and the onset and evolution of magnetic reconnection.

Energized  $O^+$  has a major impact on the onset and evolution of magnetic reconnection. The presence of energized  $O^+$  causes a two-regime onset response in a thinning current sheet. As energization increases in the lower-regime, reconnection develops at a single primary X-line, increases time-to-onset, and suppresses the rate of evolution. As energization continues to increase in the higher-regimes, reconnection develops at multiple X-lines, forming a stochastic plasmoid chain; decreases time-to-onset; and enhances evolution via a plasmoid instability. Energized  $O^+$  drives a depletion of the background  $H^+$  around the central current sheet. As the energization increases, the current sheet thinning begins to slow and eventually reverses, leading to disruption of the current sheet via a plasmoid instability.

**1 Introduction****1.1 Background**

Magnetic reconnection plays a vital role in the behavior of magnetized plasmas in Earth's magnetosphere, the Sun, magnetically confined plasmas, and across the Universe. Understanding reconnection as a fundamental physical process is already a high priority of the space physics community. It is the primary science objective of the Magnetospheric Multiscale (MMS) Mission launched in March 2015.  $O^+$  is present throughout the magnetosphere in varying quantities. While heavy ions such as oxygen are known to influence the reconnection process in the Earth's magnetosphere, their influence remains one of the many aspects of magnetic reconnection that is poorly understood. There is no agreement on the degree to which, or precisely how, heavy ions affect the dynamics of magnetic reconnection. In addition, despite the presence of energized  $O^+$  along with thermal energies, simulation studies of reconnection have been conducted exclusively with thermal heavy ions, neglecting energized heavy ions.

**1.2 Current Sheet Thinning to Onset - Expected Behavior**

Research on the theory, observation, and simulation of magnetic reconnection in laboratories and in space has a long history. Zweibel and Yamada (2016), Pontin (2020) and their cited references provide excellent overviews of the history and recent understanding of magnetic reconnection. Setting aside specific models and conditions, one can describe the basic evolution of magnetic reconnection beginning in the context of a simplified thinning current sheet (CS). Note that such a simplified description does not include all phenomena present in a physical reconnection system. A simplified anti-parallel magnetic field system, such as the configuration used here, allows for a comparison of variations in individual parameters such as composition, energization, density and CS

61 thickness. Our basic configuration does not include guide fields ( $B_y$ ) or major  $B_z$  com-  
62 ponents.

63 Dayside reconnection, between the closed magnetic field lines of the Earth and those  
64 of the Sun, produces regions of open field lines connecting the Earth and Sun. With one  
65 end fixed at the Earth, these field lines are convected past the Earth by the solar wind,  
66 and accumulate in the lobes of the magnetotail. The two lobe regions of "frozen-in" mag-  
67 netized plasma "wrap" around the Earth and meet anti-Sunward to form the magne-  
68 totail. The frozen-in condition existing in these lobes prevents the magnetic field lines  
69 in these regions from merging. Where the lobes press against one another, a thick bound-  
70 ary forms, which is called the plasma sheet or layer. Embedded within the plasma sheet  
71 a current sheet (CS) forms along the magnetic reversal (neutral) between the lobes. A  
72 duskward current of charged particles move in opposite directions (ions duskward and  
73 electrons dawnward) perpendicular to the magnetic field lines. The structure of this cur-  
74 rent sheet provides an additional barrier to the merging of the two regions. The buildup  
75 of plasma and flux in the lobes "compresses" the current sheet, causing an increase in  
76 the external to internal pressure. Generally, this forces thinning of the current sheet over  
77 time and leads to conditions favorable to magnetic reconnection. Additionally, condi-  
78 tions may arise in which a degradation and disruption of the current sheet also leads to  
79 conditions favorable to magnetic reconnection.

80 We present a description of the expected behavior of a thinning and reconnecting  
81 current sheet using the features and terminology of the magnetotail. It is intended to  
82 aid in the evaluation of our simulations by providing features for comparing the evolu-  
83 tion. Earth's magnetotail falls into the general category of a collisionless plasma based  
84 on the plasma parameters and system size. Ultimately, these parameters rely on the plasma  
85 ion content and magnetic field conditions in and around the current sheet. These condi-  
86 tions cause magnetic reconnection to occur in one of two configurations; with a single  
87 X-line or with multiple X-lines (Ji & Daughton, 2011). This depends on where the  
88 effective plasma size lies in terms of a critical transition size  $\lambda_{crit}$ . Those systems with  
89  $\lambda < \lambda_{crit}$  evolve with a single X-point, while systems with  $\lambda > \lambda_{crit}$  evolve with mul-  
90 tiple X-points. While not based on analytical theory, a  $\lambda_{crit} \approx 50$  is empirically derived  
91 (Daughton et al., 2006).

92 The thickness of the central CS is governed by the balance of its internal pressure  
93 with both magnetic and plasma pressure from the bulk (lobe) regions above and below  
94 it. Thinning occurs due to the external pressure from the lobes as flux and plasma build  
95 up around the central CS. As the CS thins, resistive instabilities form, initiating local-  
96 ized fluctuations. Once appropriate dissipative conditions are present, field lines from  
97 opposite lobes merge, altering the topology and releasing previously frozen-in energy. The  
98 field lines in the magnetotail lobes are open, i.e., connected from the Earth to the solar  
99 wind (the Sun). Once tail field lines have reconnected, they are closed, i.e., connected  
100 Earth to Earth.

101 Two-dimensional magnetic reconnection can commence ("reach onset") by vari-  
102 ous instability mechanisms. These mechanisms have been organized into a "phase diagram"  
103 based on two key dimensionless parameters (Ji & Daughton, 2011). These parameters  
104 govern which instability becomes dominant and how a system undergoing magnetic re-  
105 connection will evolve. First is the Lundquist number,  $S = 4\pi\nu_A L_{sp}/\eta c^2$ , where  $\nu_A$  is  
106 the Alfvén velocity and  $\eta$  is the plasma resistivity. Second is the scaled macroscopic sys-  
107 tem size,  $\lambda = L/\rho_s$  (not to be confused with the collisional mean-free path  $\lambda$ ), where  $L_{sp}$   
108 is the half length of the system and  $\rho_s$  is the ion sound gyroradius. Depending on the  
109 value of these two parameters, magnetic reconnection in the magnetotail can reach on-  
110 set via single or multiple X-line generation.

111 **Single X-line:** Energy from the magnetic field reconfiguration accelerates the  
112 previously frozen-in plasma out of the reconnection region. Additionally, this release of

113 magnetic tension caused by the new topology of the field lines carries the reconfigured  
 114 magnetic flux away from the reconnection region, lowering the pressure. This causes the  
 115 higher pressure plasma in the lobes to "feed" into the reconnection region.

116 When studied in a 2.5D (2D spatial and 3D fields and particle velocities) context,  
 117 the magnetic reconnection region produces several characteristic signatures in its evo-  
 118 lution.

- 119 • A magnetic field X-line, at the center of the reconnection region where thinning  
 120 has occurred.
- 121 • Along the X-line, electron-ion decoupling (Hall effect) takes place at the scale length  
 122 of ions (e.g., protons or  $O^+$ ) (Zweibel & Yamada, 2016). This generates an out-  
 123 of-plane quadrupole Hall magnetic field ( $B_y$ ) around the X-point. This also gen-  
 124 erates a large out-of-plane Hall electric field ( $E_y$ ) in the diffusion region. This is  
 125 referred to as the reconnection electric field.
- 126 • Bulk in-flow occurs, from the regions of magnetized plasma above and below the  
 127 CS (lobes), towards the X-line.
- 128 • Outflow jets of streaming ions, electrons, and magnetic flux flow away from the  
 129 X-line perpendicular to current flow in the CS.

130 **Multiple X-line:** Compared to the overall amount of studies done on 2D recon-  
 131 nection, the study of the onset of magnetic reconnection due to the secondary tearing  
 132 (plasmoid) instability is still in its growth phase. The authors are currently unaware of  
 133 any published studies on the effect of heavy ions, thermal or energized, on the evolution  
 134 of plasmoid chains.

135 Multiple X-lines may form producing "plasmoids" also called magnetic islands in  
 136 2D (also "flux ropes" in 3D) in the CS. We use islands to refer to smaller features that  
 137 do not drive system evolution as a primary X-point would. We use plasmoids to refer  
 138 to large structures that dominate the CS.

139 Secondary current sheets form between plasmoids. Secondary tearing instabilities  
 140 trigger additional magnetic reconnection that causes plasmoids to coalesce. Over time,  
 141 multiple levels of secondary reconnection can occur. In each level, a different scale size  
 142 leads to variations in the local Lundquist number, resulting in varied local rates of re-  
 143 connection. This causes the amount of reconnected magnetic flux to increase at a rate  
 144 faster than in single X-line reconnection.

145 Daughton et al. (2009) found that for magnetic reconnection generating a plasmoid  
 146 chain, the number of plasmoids,  $N$ , increased with the Lundquist number as  $S^{0.6}$ . This  
 147 trend agrees with magnetohydrodynamic (MHD) theory by Loureiro et al. (2007) who  
 148 found  $N$  increases as  $S^{3/8}$ . Additionally, Daughton et al. (2009) found that the time-to-  
 149 onset decreases with an increasing Lundquist number as  $S^{-0.5}$ .

### 150 1.3 Thermal Oxygen and Magnetic Reconnection

151 Until now, simulations of magnetic reconnection involving oxygen have focused ex-  
 152 clusively on a uniform thermal oxygen background (Hesse & Birn, 2004; Karimabadi et  
 153 al., 2011; Markidis et al., 2011; Tenfjord et al., 2019; Liang et al., 2016, 2017). Oxygen  
 154 has been treated the same as larger protons, which produce the same behavior, only on  
 155 a larger scale. No published studies involving heavy ions and plasmoid instability recon-  
 156 nection are known to us. Background thermal oxygen has limited effects on the overall  
 157 evolution of reconnection, simply acting as a "bigger" proton, maintaining about the same  
 158 effects. The higher mass directly affects the Alfvén speed leading to the two primary ef-  
 159 fects of thermal  $O^+$  on reconnection. First, thermal oxygen scales the structure of the  
 160 reconnection region to a physically larger size while maintaining the same diffusion re-

161 gion aspect ratio. Second, it appears to slow the rate of reconnection, although some have  
 162 reported that heavy ions increase the reconnection rate.

163 Winglee (2004) indicates that in his global multi-fluid modeling of the magneto-  
 164 tail, the heavy ions introduce an inherently larger-scale length to the system. The ion  
 165 cyclotron scale is important to the dynamics of the magnetosphere, especially the pres-  
 166 ence of the heavy ionospheric ions. Since heavy ions become the first to demagnetize,  
 167 they are critical to the formation of the diffusion region around the reconnection region.  
 168 In addition, localized density enhancements and depletions are seen in the tail where the  
 169 local heavy ion density can be substantially elevated. Because of these local density vari-  
 170 ations, reconnection across the tail is inhomogeneous. Winglee (2004) deals with global  
 171 magnetotail dynamics as opposed to local reconnection system behavior. This increase  
 172 in system scale is attributed to the increased mass, which enhances the changes in gyro-  
 173 radius and Alfvén speed.

174 Wiltberger et al. (2010) states that the  $O^+$  of ionospheric origin changes the re-  
 175 connection rate as evidenced by a 6-min delay in the final release of the first plasmoid.  
 176 The reconnection rate is proportional to the Alfvén speed in the fluid flowing into the  
 177 reconnection diffusion region. Therefore a reduction in the reconnection rate is expected  
 178 in the simulation with [ionospheric] outflow owing to the reduction in Alfvén speed caused  
 179 by the  $O^+$  ions in the lobe inflow region. Tenfjord et al. (2019) found that the presence  
 180 of thermal  $O^+$  (or other heavy ions) significantly decreases the reconnection rate, while  
 181 the temperature (1.0 keV and 0.2 keV) has no significant effect. One common result of  
 182 the presence of  $O^+$  in collisionless reconnection is the increased scaling of the quadrupole  
 183 structure and dimensions of the diffusion region; however, the effect on the reconnection  
 184 rate is not clear Liu et al. (2015). Acceleration of thermal  $O^+$ , due only to the recon-  
 185 nection electric field and not external to the reconnection process was noted (Karimabadi  
 186 et al., 2011; Liu et al., 2015).

187 Multiple studies have touched on the effects of heavy ions on the rate of reconnec-  
 188 tion in the magnetosphere: Shay et al. (2007) using a 2D, 3-fluid model; Markidis et al.  
 189 (2011) using a 2.5D PIC; and Karimabadi et al. (2011) using a 2D PIC simulation. Shay  
 190 et al. (2007) and Karimabadi et al. (2011) reported a marked decrease in the rate of mag-  
 191 netic reconnection due specifically to the presence of oxygen in the inflow region. Hesse  
 192 and Birn (2004) concluded that background oxygen does not strongly restrict the recon-  
 193 nection rate. Markidis et al. (2011), (Hesse & Birn, 2004) and Karimabadi et al. (2011)  
 194 reported that the presence of an  $O^+$  population slightly decreases the reconnection rate.  
 195 Baker et al. (1982) and Liu et al. (2013) argue from observational data that  $O^+$  may be  
 196 increasing the reconnection rate. Although most of the evidence indicates slowing, there  
 197 is still some disagreement as to what kind of effect the presence of heavy ions has on the  
 198 reconnection rate.

#### 199 1.4 Energized Oxygen

200 Although observed in-situ (Kistler et al., 2005), magnetic reconnection in the pres-  
 201 ence of an *energized*  $O^+$  background has not previously been investigated via kinetic PIC  
 202 simulations. Other than studies of acceleration produced by magnetic reconnection it-  
 203 self, and our work on energized  $O^+$  bifurcation (George & Jahn, 2020), no previous work  
 204 has performed kinetic plasma simulations that included energized  $O^+$ . The work pre-  
 205 sented here is motivated by observations of energized  $O^+$  in the magnetotail together  
 206 with a lack of corresponding simulation studies of magnetic reconnection involving en-  
 207 ergized oxygen. Kronberg et al. (2014) gives an excellent overall review of the transport  
 208 and acceleration (energization) of heavy ions in the magnetosphere and magnetotail.

209 The dawn-dusk electric field across the magnetotail CS predicts cross-tail ion ac-  
 210 celeration as evidenced by an increased dusk-side asymmetry of energized ions (Speiser,  
 211 1965; Lyons & Speiser, 1982; Meng et al., 1981). Several investigations of cross-tail elec-

212 tric field acceleration of protons and  $O^+$  have been undertaken resulting in acceleration  
 213 estimates of  $>50$  keV  $O^+$  (Birn et al., 2004), 100-200 keV  $H^+$  (Birn & Hesse, 1994), 20  
 214 keV  $O^+$  (Ipavich et al., 1984), 50-500 keV  $H^+$  (Meng et al., 1981), and 112-157 keV  $O^+$   
 215 (Wygant et al., 2005). Without regard to the acceleration mechanism, energized  $O^+$  in  
 216 the 12 to 40 keV range has been observed by (Kistler et al., 2005) streaming dawn to  
 217 dusk in the magnetotail at about 19 RE. While the streaming  $O^+$  is identified as non-  
 218 adiabatic, there is no mention of the CS structure or presence of a bifurcation.

## 219 1.5 Preview of our work

220 The following sections report our studies of energized  $O^+$  in the magnetotail and  
 221 its effect on magnetic reconnection. We previously reported the creation of a bifurcated  
 222 current sheet (BCS) due to a single population of Speiser-orbiting heavy ions (George  
 223 & Jahn, 2020). Here we focus on a thinning CS in the presence of energized  $O^+$  and its  
 224 effect on the onset and evolution of magnetic reconnection. We use a simplified magne-  
 225 totail system configuration with oppositely directed magnetic field lines above and be-  
 226 low the central CS. This makes the cross-tail potential, and thus the natural energiza-  
 227 tion of ions, duskward. As such it is natural for an energized ion to travel along a Speiser  
 228 orbit and for a population of energized ions to form a BCS.

229 In §2, we present the methodology followed to simulate the thinning current sheet  
 230 with energized  $O^+$  present. This includes the simulation code we used, the setup and  
 231 parameter space we cover, and the analysis methods we apply to the simulation outputs  
 232 to understand the system behavior. After this, in §3, we present the results of these sim-  
 233 ulations, starting with our baseline runs, then runs with variable  $O^+$  energization, and  
 234 finally runs with different  $O^+$  density and CS thickness. We began our study by com-  
 235 paring the results of our simulations to those of published kinetic simulation studies in-  
 236 volving two-species and three-species magnetic reconnection with thermal background  
 237 ions. With these comparisons validating our setup, we introduced energized  $O^+$  to the  
 238 basic magnetotail model. Although a physical magnetotail model contains more com-  
 239 plex features, we excluded any major  $B_z$  and guide field components for ease in isolat-  
 240 ing results. This simple magnetotail model is in keeping with those used in previous ki-  
 241 netic studies. We purposely kept the system configuration simple to aid in the exami-  
 242 nation of this new area of simulation research. Our goal was not to produce a definitive  
 243 study but to lay foundations for and justify further investigations into the effects of en-  
 244 ergized  $O^+$  on magnetic reconnection. Then, in §4 we discuss what these simulations show  
 245 and examine effects that result from our simulation environment and those that repre-  
 246 sent the physics involved. This includes the parameter space of varying energization and  
 247 density of the  $O^+$  as well as the current sheet thickness.

## 248 2 Simulation Methodology

249 We performed three-species, 2.5D, Particle-In-Cell (PIC) simulations of a thinning  
 250 CS leading to magnetic reconnection. Our simulations are similar in setup to PIC stud-  
 251 ies of thermal  $O^+$  found in Table 1, extending our previous studies of energized  $O^+$  form-  
 252 ing a BCS over a thinning central  $H^+$  CS (George & Jahn, 2020).

253 While not a physical representation of either the magnetosphere or the magneto-  
 254 tail, we refer to the simulations as being a magnetotail-like system oriented in the Geo-  
 255 centric Solar Magnetospheric (GSM) coordinate system. Using the Harris equilibrium  
 256 for a magnetotail-like system follows previous  $O^+$  PIC simulations. The simulation re-  
 257 gion is oriented to correspond to the GSM X-Z plane in the center of Earth's magneto-  
 258 sphere at  $Y=0$ . Y corresponds to the GSM Y duskward direction and out-of-plane di-  
 259 rection.

Our simulations begin with a CS centered between two regions of plasma in anti-parallel magnetic fields (anti-parallel indicating here that there are no guide-fields or major  $B_z$  components to the magnetic field). This is the well-known, commonly used, Harris equilibrium configuration (Harris, 1962). This follows previous PIC simulations of 3-species,  $O^+$ , plasmas to reduce variability at early stages of energized  $O^+$  investigations (George & Jahn, 2020). Our simulations, listed in Table 1, contain a three-species plasma representing electrons, protons and heavy ions. Following our previous work, we modified the three-species thermal plasma by adding a small duskward velocity component. We assume that that energization stems from the cross-tail electric field (§1.4), although this is not the only possible source of energization in the magnetotail. A single two-species simulation (Run 1) and two, three-species, simulations with thermal  $O^+$  (Run 2 and Run 3) serve as a baseline for comparisons to previous simulation studies.

## 2.1 PIC Code

Our investigation uses a 2.5D, fully electromagnetic, implicit PIC code described in detail in Hesse and Schindler (2001). In a 2.5D simulation the particle positions are calculated in 2D while the particle velocities, electric fields and magnetic fields are calculated in 3D. Hence the designation of 2.5D. This has been used extensively in previous plasma studies involving reconnection, and specifically in our precursor study of  $O^+$  BCS (George & Jahn, 2020). Simulations involving thin CS and magnetic reconnection have been performed extensively using PIC codes (Hesse et al., 2001; Hesse & Birn, 2004; Hesse et al., 1999; Hesse & Schindler, 2001; Karimabadi et al., 2011; Shay et al., 2007; Markidis et al., 2011; Tenfjord et al., 2019; Liang et al., 2016, 2017). An explanation of this code can be found in the precursor work and its references (George & Jahn, 2020). The same computational platform described there was used for this work.

## 2.2 Simulation Setup

We use two simulation box sizes. The larger box is double the size of the smaller along the z-axis, i.e., perpendicular to the CS. The larger box was used to remove boundary interactions identified in the smaller box simulations. The smaller box is 320 x 80 proton inertial lengths, with a computational grid size of 800 x 400 cells. The larger box is 320 x 160 proton inertial lengths with a computational grid size of 800 x 800 cells.

The boundary conditions have been set along the x-axis and z-axis, in keeping with PIC simulations referenced previously. For particles, the X boundaries are periodic. Any particle exiting one side reenters the opposite side with the same velocity vector. The Z boundaries are specularly reflecting. Any particle exiting the +/-Z boundary reenters at the same location but with the opposite  $v_z$ . For the electric and magnetic fields the X boundaries are periodic and continuous. The Z boundaries are simple, reflecting boundaries for the electric and magnetic fields. This is accounted for in the implicit integration performed in the field calculations. Scaling and normalization of simulation parameters is unit-less. Lengths are normalized to the proton inertial length ( $c/\omega_{pi}$ ), while time is normalized to the proton gyroperiod. The ratio between the electron plasma and gyrofrequencies is 5:1. This establishes the relationship between  $B_o$  and  $n_o$  where  $B_o$  is the peak magnetic field strength in the surrounding bulk plasma and  $n_o$  is the initial peak density at the center of the CS. A background density of 0.1  $n_o$  was used for the  $H^+$  in all runs. A background density of 0.1  $n_o$  was used for the  $O^+$  in all runs except Run 20 and Run 21, which used a density of 0.05  $n_o$ .

## 2.3 Mass Ratios

In an ideal simulation, the relative masses of the species would reflect physical ratios. This is both computationally prohibitive and unnecessary. Our study uses  $m_e:m_{H^+}:m_{O^+}$  mass ratios of 1:25:250. Previous kinetic studies have shown that these mass ratios, while

309 not physical, are more than sufficient to separate the mass effects of electrons and pro-  
 310 tons as well as to study oxygen dynamics. While physical mass ratios are not used in  
 311 this investigation, the lighter ions represent protons, hydrogen or  $H^+$ , and the heavy ions  
 312 represent oxygen or  $O^+$ .

313 Kinetic simulations using the same Harris equilibrium and  $m_p/m_e$  mass ratios of  
 314 25:1, 180:1 and 1836:1, revealed no effect on the larger-scale phenomena (Ricci et al., 2002);  
 315 The evolution of two-species reconnection was nearly identical for  $m_p:m_e$  of 9:1, 25:1,  
 316 64:1, and 100:1 (Hesse et al., 1999), with a  $m_p:m_e$  ratio of 25:1 separating the relevant  
 317 electron physics from the proton physics. The results of Markidis et al. (2011), who used  
 318 physical masses, was in agreement with those of Karimabadi et al. (2011) and Hesse and  
 319 Birn (2004), who used reduced mass ratios. All reported a separation of scale between  
 320 the three species for studies of both pre- and post-reconnection evolution.

## 321 2.4 $O^+$ Energization

322 Previous simulation studies of reconnection involving  $O^+$  focused exclusively on  
 323 thermal  $O^+$  (Markidis et al., 2011; Hesse & Birn, 2004; Karimabadi et al., 2011; Ten-  
 324 fjord et al., 2019; Liang et al., 2016, 2017). Other than baseline simulations with ther-  
 325 mal  $O^+$ , our simulations use  $O^+$  initial conditions that are distinctly different. We use  
 326  $O^+$  that is energized as opposed to thermal. Run 2 and Run 3 are initialized with a ran-  
 327 dom thermal distribution of 0.5 keV. Tenfjord et al. (2019) demonstrated no significant  
 328 effect in reconnection rate between runs with background  $O^+$  temperatures of 200 eV  
 329 and 1 keV.  $O^+$  energization is achieved by adding a  $v_y$  distribution to this thermal en-  
 330 ergy upon initialization of the simulation. This velocity approximates the acceleration  
 331 that would be introduced by the cross-tail electric field. Giving the  $O^+$  an initial veloc-  
 332 ity is an oversimplification, yet it naturally places the entire population into Speiser or-  
 333 bits forming a bifurcated current sheet (George & Jahn, 2020). Energization values of  
 334 the  $O^+$  in the system were chosen to be in a range that has been observed in-situ, but  
 335 has never been investigated via kinetic PIC simulation (Kistler et al., 2005). Energiza-  
 336 tion of the  $O^+$  results in the formation of a BCS sheet that is essentially superimposed  
 337 over the central CS (George & Jahn, 2020). In each case, the simulation is allowed to  
 338 evolve to the point at which magnetic reconnection is fully developed. Evolution of the  
 339 magnetic reconnection in each case is compared to determine the overall effect on the  
 340 system.

## 341 2.5 Reconnection Onset and Rate

342 Several features can be used to establish the point at which the onset of magnetic  
 343 reconnection occurs in a simulation. Onset accompanies the formation of one or more  
 344 X-lines or X-points. This indicates that magnetic field lines that were previously directed  
 345 opposite one another (anti-parallel) have begun to merge. This alters their fundamen-  
 346 tal topology and increases the overall  $B_z$  component of the magnetic field, Onset is also  
 347 indicated by the formation of a reconnection electric field located at the center of this  
 348 X-line. Additionally, onset can be identified by the formation of an out-of-plane quadrupole  
 349 magnetic field ( $B_y$ ). A common method for identifying X-line formation is to calculate  
 350 the amount of reconnected magnetic flux (reconnected flux or flux herein) or  $\Phi(t)$  found  
 351 in Equation 1. Initial magnetic field lines are oriented parallel to the x-axis and as such  
 352 have only  $B_x$  components. As an X-line is formed, the field line topology changes such  
 353 that there is an increase of  $B_z$ . We use three parameters based on the reconnected mag-

**Table 1.** Simulation Runs Performed:

Run	$O^+$ Energy	Onset @ time step	Box Size
1	No $O^+$	630	320 x 80
2	thermal $O^+$	1,422	320 x 80
3	thermal $O^+$	1,474	320 x 160
4	0.7 keV	1,615	320 x 80
5	3.5 keV	2,725	320 x 80
6	5.25 keV	3,698	320 x 80
7	6.125 keV	4,830	320 x 80
8	7.0 keV	6,207	320 x 80
9	7.875 keV	7,500	320 x 80
10	8.75 keV	9,539	320 x 80
11	10.5 keV	8,373	320 x 80
12	14.0 keV	5,162	320 x 80
13	17.5 keV	2,443	320 x 80
14	0.7 keV	2,560	320 x 160
15	3.5 keV	5,454	320 x 160
16	5.25 keV	14,937	320 x 160
17	6.125 keV	20,870	320 x 160
18	7.0 keV	24,601	320 x 160
19	7.875 keV	25,690	320 x 160
20	8.75 keV	22,143	320 x 160
21	10.5 keV	14,854	320 x 160
22	14.0 keV	7,194	320 x 160
23	17.5 keV	4,223	320 x 160
24	7.0 keV	1,783 *	320 x 80
25	14.0 keV	3,311 *	320 x 80
26	7.0 keV	no onset **	320 x 80
27	14.0 keV	5,600 **	320 x 80
28	7.0 keV	1,860 ***	320 x 80

\* lower density ( $0.05 n_o$ ), \*\* thicker CS, \*\*\* thinner CS

354 netic flux: instantaneous, differential and integrated flux.

$$\text{Instantaneous Reconnected Flux : } \Phi(t) = \frac{\int_{\mathbf{x}} |\mathbf{Bz}(\mathbf{x}, \mathbf{z} = \mathbf{0}, t)| d\mathbf{x}}{\int_{\mathbf{x}} d\mathbf{x}} \quad (1)$$

355 The instantaneous flux,  $\Phi(t)$  (Equation 1), is an indication of the current state of the  
356 system evolution at a given time. As the flux changes, reconnection or merging has pro-  
357 gressed. Generally,  $\Phi(t)$  is calculated between O-points and X-points, (Hesse & Birn, 2004;  
358 Markidis et al., 2011), however, in our study multiple X-points can occur simultaneously.  
359 In this case,  $\Phi(t)$  is calculated by taking the integral of the  $|B_z|$  component along the  
360 current sheet (Equation 1). Increases in  $\Phi(t)$  indicate  $B_x$  field lines reconnecting into  $B_z$   
361 field lines.  $\Phi(t)$  generally increases over time, however, this is not always true. Decreases  
362 in  $\Phi(t)$  indicate the opposite with  $B_z$  field lines reconnecting into  $B_x$  field lines. This  
363 occurs when islands dissipate or plasmoids coalesce. Even though  $\Phi(t)$  is decreasing, re-  
364 connection is proceeding. Additionally, we normalize this value to the magnetic field scal-  
365 ing factor  $B_o c/\omega_{pi}$ . This method is easily adapted to different tearing modes and does

not rely on locating a specific point in the inflow or outflow regions. To give numerical consistency and to allow for comparison between runs,  $\Phi(t)$  was used as an indicator to establish the point of onset of reconnection. At each time step, the magnitude of  $|B_z|$  was integrated along the magnetic null ( $z = 0$ ) for all cells along the x-axis. This integral was then scaled according to the number of grid cells along the x-axis of the simulation box. A numerical threshold value of  $0.005 B_o$  was selected for the "point of onset" as a common point of comparison. The reconnected flux reaching this threshold is our definition for the point of onset, herein referred to as the time-to-onset. This value was chosen such that the reconnected flux increased monotonically (near the point of onset) after exceeding the threshold.

$$\text{Differential Reconnected Flux : } \Delta\Phi(t) = \frac{|\Phi(t + \Delta t) - \Phi(t)|}{\Delta t} \quad (2)$$

The differential flux,  $\Delta\Phi(t)$  (Equation 2), is an indication of the rate at which the system is evolving. The  $\Delta\Phi(t)$ , is the change in  $\Phi(t)$  per unit time and is also referred to as the reconnection rate. There are several methods to determine the reconnection rate. These rely on the type of reconnection model assumed, specifically, the overall topology of the evolution. Methods include the use of the reconnection electric field or the inflow and outflow Alfvén speeds (Comisso & Bhattacharjee, 2016). These methods are generally dependent on selecting the correct location to perform calculations. Here we use the most basic definition of the reconnection rate: the amount of magnetic flux reconnecting per unit time. We previously calculated the flux,  $\Phi(t)$ , which gives an indication of how much magnetic flux has transitioned between  $B_x$  and  $B_z$  field line components. The differential change of reconnected flux with respect to time,  $\Delta\Phi(t)$ , is then the amount of reconnecting flux per unit time (Equation 2). The reconnection rate is an indication of how fast the system is evolving. We normalize the differential flux to the bulk magnetic field value and the proton Alfvén speed,  $B_o\nu_A/c$ . To calculate  $\Delta\Phi(t)$ , we evaluate  $\Phi(t)$  at two points in time and divide by this difference in time. For a common point of comparison, we selected a difference of 10 time steps taken at a point 1,000 time steps after onset.

$$\text{Integrated Reconnected Flux : } \Sigma\Phi(t) = \sum_0^t \Phi(\tau) \quad (3)$$

The integrated flux,  $\Sigma\Phi(t)$  (Equation 3), is a proxy of the global effectiveness of the system evolution. It is representative of the total amount of flux converted via reconnection. As the value of  $\Phi(t)$  increases, so does  $\Sigma\Phi(t)$ , indicating reconnection is progressing.  $\Phi(t)$  generally increases over time, however this is not always true. As the value of  $\Phi(t)$  decreases,  $\Sigma\Phi(t)$  also increases. This decrease corresponds to a reduction in the  $B_z$  component across the current sheet. Physically this can occur via the dissipation of an island in the reconnection outflow, or by the coalescing of plasmoids. Since magnetic reconnection is not a reversible process, any change in the  $B_z$  component (i.e., back to  $B_x$  component) constitutes an increase in overall energy transfer.  $\Sigma\Phi(t)$  is normalized the same way as the  $\Phi(t)$ .

### 3 Results

Our work began by generating baselines of our simulation setup with backgrounds of both  $H^+$  (Run 1) and thermal  $O^+$  (Run 2 and Run 3). For validation of our simulation setup, we compared these baselines against expected behavior from published research of a thinning CS undergoing magnetic reconnection. We then performed ten simulations (Run 4 through Run 13), with varying energization applied to the  $O^+$  background.

409 The simulation box size was doubled in the z-dimension to address a small but quan-  
 410 tifiable boundary interaction in the smaller box. We performed an additional ten, oth-  
 411 erwise identical, simulations (Run 14 through Run 23) using the larger simulation box.  
 412 We finally performed five simulations (Run 24 through Run 28) with variations of  $O^+$   
 413 density and CS thickness to evaluate any effect on the system.

414 Based on the simulations we computed three analysis parameters, described in sec-  
 415 tion §2.5, based on the amount of reconnected magnetic flux. These parameters were in-  
 416 stantaneous flux,  $\Phi(t)$ , differential flux,  $\Delta\Phi(t)$ , and integrated flux,  $\Sigma\Phi(t)$ . Then, based  
 417 on  $\Phi(t)$  crossing a threshold value, we determined the time-to-onset for each simulation.

418 The results of these simulations and calculations are presented below. First we present  
 419 the two baseline simulations performed for validation. Next are observations made of two  
 420 of the simulations, one performed at 7.0 keV and the other 14.0 keV. Then, we present  
 421 the results of the reconnected magnetic flux calculations. Finally, we present the find-  
 422 ings from the time-to-onset determination followed by a discussion of the results.

### 423 3.1 Two-Species (no $O^+$ )

424 For the first baseline simulation of our investigation, we validated our simulation  
 425 setup (Run 1) against a two-species, proton-electron simulation of a thinning CS. Our  
 426 setup was based on the well-known Geospace Environmental Modeling (GEM) Recon-  
 427 nection Challenge (Birn et al., 2001). This challenge produced an excellent array of com-  
 428 parable results of two-species reconnection in a common configuration (Birn & Hesse,  
 429 2001; Hesse et al., 2001; Otto, 2001; Pritchett, 2001; Shay et al., 2001). The GEM chal-  
 430 lenge included an initial finite perturbation in the CS to speed up the dynamics. The  
 431 rationale for such an initial perturbation was to put the system in the non-linear regime  
 432 of magnetic reconnection from the beginning of a simulation (Birn et al., 2001). Run 1  
 433 began with the same GEM configuration but without the perturbation such that the CS  
 434 would thin naturally. While this required longer simulation times, it allowed compar-  
 435 ison with our configuration runs that added  $O^+$ . As a result, in Run 1, multiple tear-  
 436 ing instabilities formed in the central CS, however only one primary X-point fully de-  
 437 veloped.

438 Results of our two-species simulation (Run 1) were consistent with the simulations  
 439 of published studies. The evolution described in §1.2 occurred as expected. It was char-  
 440 acterized by a single primary X-point, with a slow increase in reconnected magnetic flux  
 441 and a generally smooth evolution.

442 Figure 1 shows the evolution and features confirming the expected results. Frames  
 443 a) and b) show the formation of a primary X-point where reconnection is taking place.  
 444 There are also small secondary islands in the outflow jets forming smaller X-point re-  
 445 connection sites. Frame c) indicates the inflow of background protons into the X-point  
 446 of the reconnection region. Frame d) indicates the outflow jets of protons along the CS.  
 447 Frame f) shows the well defined out-of-plane ( $B_y$ ) quadrupole magnetic field. Since there  
 448 were no indications of boundary interference, no equivalent of Run 1 was made in a larger  
 449 box.

### 450 3.2 Three-Species (Thermal $O^+$ )

451 We validated our baseline three-species, ( $O^+$ ,  $H^+$ ,  $e^-$ ) simulation (Run 2) against  
 452 published works (Hesse & Birn, 2004; Karimabadi et al., 2011; Markidis et al., 2011; Ten-  
 453 fjord et al., 2019; Liang et al., 2016, 2017). Results of our three-species simulation with  
 454 thermal  $O^+$  (Run 2) are consistent with published studies. Figure 7 (red curves) shows  
 455 a comparison of the difference in evolution between two-species and three-species (with  
 456 thermal  $O^+$ ) simulations (Run 1 and Run 2). The time-to-onset, listed in Table 1, is de-

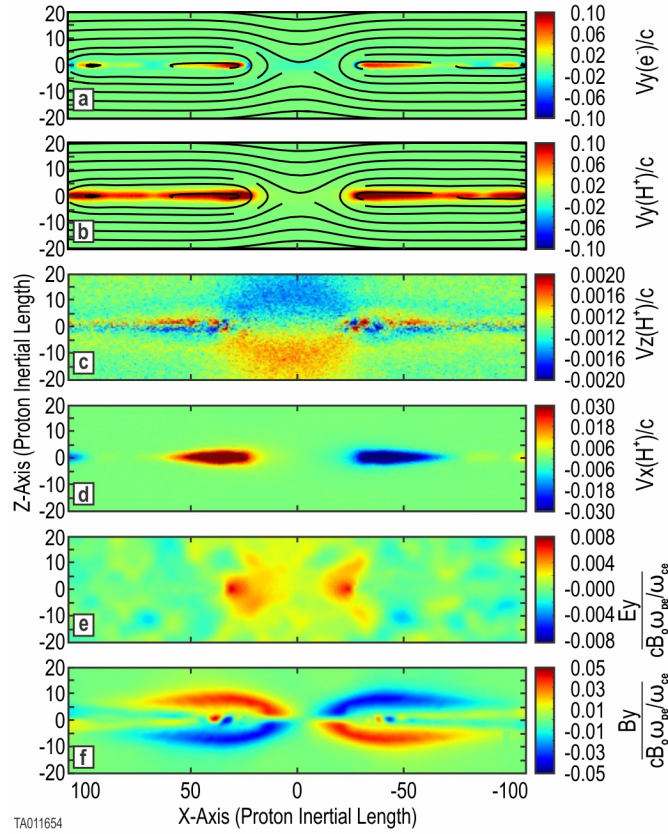


**Figure 1.** Key parameters for a two-species simulation (Run 1). Shown are 2D color plots of key system parameters at 1000 time steps ( $t=1630$ ) after onset of magnetic reconnection. Frames a) and b) are the  $j_y$  component of electron and proton current overlaid with the in-plane magnetic field lines. Frame c) shows the  $v_z$  component of the background protons. Frame d) shows the  $v_x$  component of the protons forming outlet jets. Frame e) gives the  $E_y$  component of the electric field. Frame f) provides the  $B_y$  magnetic field.

457 layed when  $O^+$  is added. There is also a small visible decrease in the rate of reconnected  
 458 flux. This is in agreement with published results.

459 While there were no indications of boundary interference, an equivalent of Run 2  
 460 was performed in a larger box (Run 3). This additional baseline was performed to val-  
 461 idate the large box simulation setup against Run 2 and the same published works men-  
 462 tioned above. The three-species thermal  $O^+$  simulations (Run 2 and Run 3) evolved ac-  
 463 cording to expectations in §1.2. The time-to-onset and reconnected flux profiles of Run  
 464 3 and Run 2 are nearly identical. Each run had multiple tearing instabilities forming in  
 465 the current sheet prior to onset, however, only one primary X-point ever developed.

466 Figure 2 shows the evolution and key features, confirming the expected results at  
 467 1,000 time steps after onset. Frames a) and b) show the formation of a primary X-point  
 468 where reconnection is taking place. Additional X-points developed into small secondary  
 469 islands in the outflow jets and did not support reconnection onset. We refer to these as  
 470 islands to distinguish their minor effect compared to that of plasmoids, which have a ma-  
 471 jor effect in evolution. Frame c) indicates the inflow of background protons towards the  
 472 X-point of the reconnection region. A color plot of  $v_z$  for the  $O^+$  ions at the same time  
 473 step (not shown) indicates  $O^+$  ions are beginning to move towards the X-point, although  
 474 much more slowly. Frame d) indicates the outflow jets of protons along the CS. The  $O^+$   
 475 outflow jets (not shown) are nearly indistinguishable from the  $H^+$  jets. Figure 3 shows  
 476 a side-by-side comparison of the out-of-plane ( $B_y$ ) magnetic field between Run 1, with

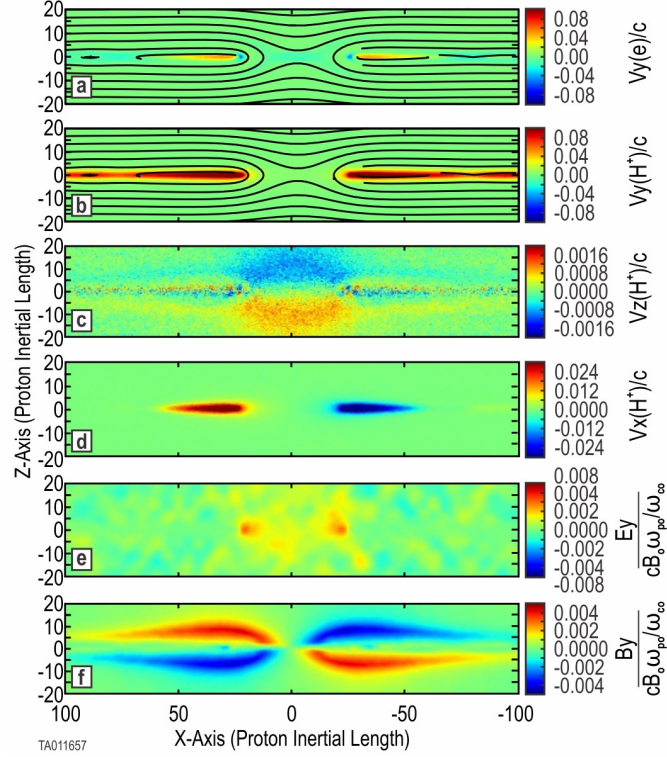


**Figure 2.** Key parameters for a three-species simulation (Run 2) with thermal  $O^+$ . Shown are 2D color plots of key system parameters at 1000 time steps ( $t=2422$ ) after onset of magnetic reconnection. Frames a) and b) are the  $j_y$  component of electron and proton current overlaid with the in-plane magnetic field lines. Frame c) shows the  $v_z$  component of the background protons. Frame d) shows the  $v_x$  component of the protons forming outlet jets. Frame e) gives the  $E_y$  component of the electric field. Frame f) provides the  $B_y$  magnetic field.

no  $O^+$ , and Run 2, with thermal  $O^+$ . For consistency each plot is taken at a the time step when instantaneous flux peaks (Figure 7). This gives an equivalent reference point in the evolution of each run. This comparison shows an increase in the scale size in the X-direction. The broadened scale of the out-of-plane quadrupole structure has been reported previously by Shay and Swisdak (2004); Karimabadi et al. (2011); Markidis et al. (2011), who show the  $B_y$  profile for their simulations without  $O^+$  and with thermal  $O^+$ . Both indicate that the heavier mass of the  $O^+$  increases both the scale and intensity of the Hall effect quadrupole structure of  $B_y$ .

### 3.3 Three-Species (Energized $O^+$ )

The sections above discuss the baseline runs used to validate our configuration. The focus of this study is to investigate the effects of energized  $O^+$  on magnetic reconnection. Here we present 25 runs that include a background of energized  $O^+$ . These runs included ten initial simulations (Run 4 through Run 13) and a second set of ten runs in a larger simulation box (Run 14 through Run 23), with otherwise unchanged conditions. Additionally, these runs include five runs with variations in the  $O^+$  density and CS thickness (Run 24 through Run 28).

Examination of the simulations indicated that the systems were evolving according to two different topologies. We present a detailed description of two cases, 7.0 keV and 14.0 keV energization, representative of each topology. In both the small box and

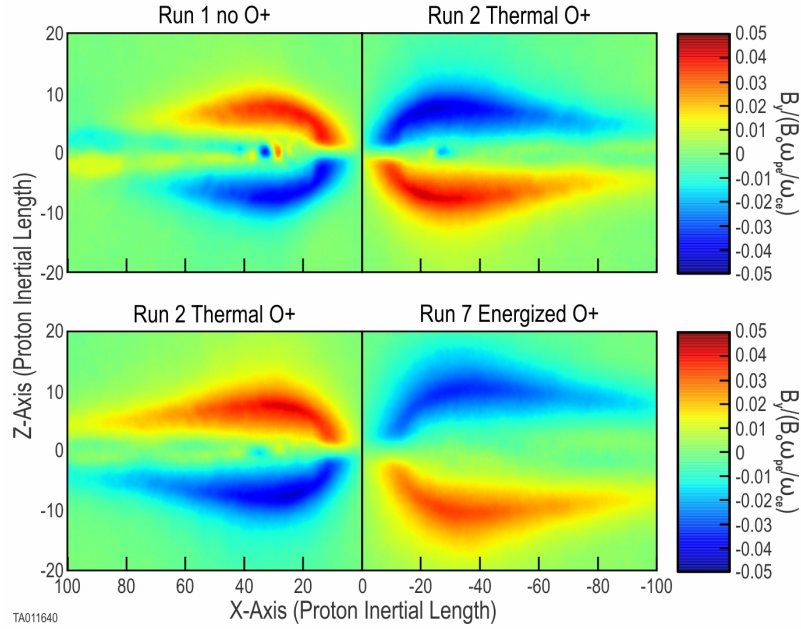


**Figure 3.** This shows color plots of the out-of-plane ( $B_y$ ) magnetic field produced aligned with the reconnection X-line. These are all taken at 1,000 time steps after onset of their respective run. On the top left is Run 1 with no  $O^+$  present. and on the top right is Run 2 with thermal  $O^+$  added. The larger scale produced by the thermal  $O^+$  is evident. On the bottom left is Run 2 with thermal  $O^+$  present. and on the bottom right is Run 8 with 7 keV energized  $O^+$ . The larger scale produced by the energized  $O^+$  is evident.

496 the large box simulations, the lower seven energizations exhibited a single primary X-  
 497 point where reconnection takes place. The higher three energizations of both simulation  
 498 sizes evolved into a multiple X-point plasmoid chain.

499 We present the effects of the energized  $O^+$  found by calculating the instantaneous,  
 500 differential, and integral flux (§3.3.3) of each simulation. We also present our results from  
 501 the determination of the time-to-onset of magnetic reconnection (§3.3.4), at the each of  
 502 various energizations,

### 503 3.3.1 7.0 keV Energization

504 Several of the runs can be characterized by the formation of a single principle X-  
 505 point along the current sheet, leading to a slow, smooth evolution. Energizations from  
 506 0.7 keV to 8.75 keV (Run 4 through Run 10 and Run 14 through Run 20) fall into this  
 507 category. The 7.0 keV simulation (Run 8) is typical and is described here. Figure 4 shows  
 508 the key parameters of Run 8, allowing us to see that it evolves similar to the baseline  
 509 simulations with no  $O^+$  and with thermal  $O^+$ .

510 We note observations made from these simulations:

- 511 • The structure of the central CS, shown in frames a) and b), is the same as that  
 512 of Run 1 and Run 2, with an X-point forming in the center of the CS. The only  
 513 major difference being the complete lack of any secondary island formation in the  
 514 outflow regions.
- 515 • Frame c) is significantly different than the baseline cases, showing a different evo-  
 516 lution of the magnetic reconnection region. The inflow of  $H^+$ , seen in Figures 1  
 517 and 2, is very near the CS at the X-point. Frame c) shows this inflow at +/-30  
 518 proton gyroradii, well away from the X-point. The  $v_z$  color plot outside (+/-X)

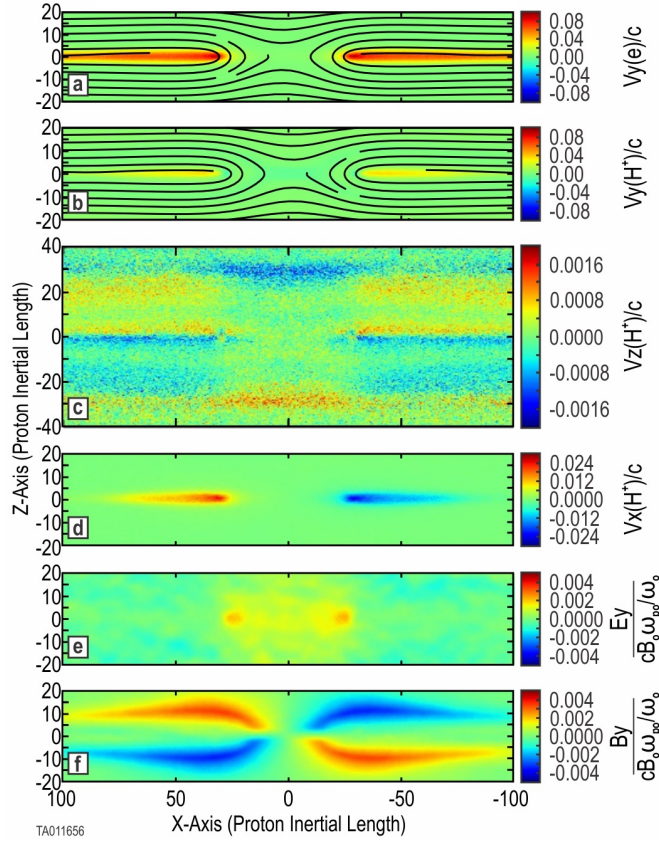


**Figure 4.** Key parameters for the 7.0 keV energized  $O^+$  simulation (Run 8). Shown are 2D color plots of key system parameters at 1,000 time steps ( $t=7207$ ) after onset of magnetic reconnection. Frames a) and b) are the  $j_y$  component of electron and proton current overlaid with the in-plane magnetic field lines. Frame c) shows the  $v_z$  component of the background protons. Frame d) shows the  $v_x$  component of the protons forming outlet jets. Frame e) gives the  $E_y$  component of the electric field. Frame f) provides the  $B_y$  magnetic field. A time sequence of the  $O^+$  BCS is shown in Figure 6.

519 of the reconnection region, shows that  $H^+$  motion is away from the CS: red to-  
 520 wards  $+Z$  and blue towards  $-Z$ . Additionally, along  $Z=0$ , there is also  $H^+$  motion  
 521 away from (or out of) the CS. As a result of this flow away from the CS, once re-  
 522 connection has begun, this places the inflow further away from the central CS. This  
 523 is in direct opposition to the  $H^+$  inflow seen in Figures 1 and 2

- 524 • Frame d) shows that the formation of  $H^+$  jets in the outflow is the same as in the  
 525 baseline cases. For the baseline cases, the  $O^+$  jets were essentially the same as the  
 526  $H^+$  jets.
- 527 • This becomes distinctly different when the  $O^+$  is energized. Figure 6 shows the  
 528 time evolution for the energized  $O^+$  in Run 8. This shows the  $v_y$  (left) and  $v_x$  (right)  
 529 components of the bifurcated CS formed by the energized  $O^+$  at three different  
 530 time steps. At time step 6,000, prior to onset, the bifurcated configuration of the  
 531  $O^+$  is unperturbed. The two horizontal lines indicate the dual distribution of  $v_y$ .  
 532 Also there is no significant  $v_x$  component. Inspection of individual particle traces  
 533 (not shown) verify that  $O^+$  moves in Speiser orbits gyro-rotating between the up-  
 534 per and lower bulk regions around the central CS. The two  $v_y$  peaks (in yellow)  
 535 in the top left frame indicate where the  $O^+$  gyro-rotates back towards the central  
 536 CS. At time step 8,000, the  $O^+$  ions have begun to turn outward. However,  
 537 they are not limited to the same outflow region (near  $Z=0$ ) as the  $H^+$  seen in Fig-  
 538 ure 4. The X-ward turning is revealed by the appearance of  $v_x$  components showing  
 539 outward velocity. Time step 10,000 shows outflow jets with a bifurcated struc-

540        ture similar to the original out-of-plane bifurcated structure in the central CS. In-  
 541        spection of individual particle traces verified that the outward turning is occur-  
 542        ring while the  $O^+$  Speiser orbits remain intact. The color plot of  $v_y$  changing to  
 543        red indicates an acceleration of the  $O^+$  in Y, which is likely due to the Speiser or-  
 544        bits passing through the reconnection electric field.

- 545        • Frame e) shows that the evolution of the reconnection electric field follows that  
 546        of Runs 1 and 2.
- 547        • Frame f) shows the development of a quadrupole out-of-plane magnetic field mir-  
 548        roring the structure of the X-point.
- 549        • The bottom frames of Figure 3 show a side-by-side comparison of the out-of-plane  
 550        ( $B_y$ ) magnetic field between Run 2 with thermal  $O^+$  and Run 7 with 7 keV en-  
 551        ergized  $O^+$ . For consistency, each plot is taken at 1,000 time steps after onset, as  
 552        listed in Table 1. This gives an equivalent reference point in the evolution of each  
 553        run. This comparison shows an increases not only in the scale size along the X-  
 554        direction, but also in the Z-direction. There is also an increase in the spacing be-  
 555        tween the poles in the Z-direction. This indicates an increased size of the recon-  
 556        nection region, not only beyond that with no oxygen, but beyond that with ther-  
 557        mal  $O^+$ .

### 558        **3.3.2 14.0 keV Energization**

559        Several of the energized  $O^+$  runs can be characterized by the formation of multi-  
 560        ple X-points along the current sheet. Energizations from 10.5 keV to 17.5 keV (Run 11  
 561        through Run 13 and Run 21 through Run 23) belong to this group. The 14.0 keV sim-  
 562        ulation (Run 22) is representative of these simulations and is described here. The prin-  
 563        cipal observation is that the CS is completely disrupted via a secondary tearing (plas-  
 564        moid) instability. A detailed examination of the evolution of a stochastic plasmoid chain  
 565        is beyond the scope of the present work. Markidis et al. (2012) provides a detailed study  
 566        via PIC simulation of reconnection in a plasmoid chain. Figure 5 shows the key param-  
 567        eters of Run 22, allowing us to see that it evolves differently than both the runs simi-  
 568        lar to Run 8 and the baseline simulations with no  $O^+$  and with thermal  $O^+$ . We note  
 569        observations made from these simulations:

570        X-lines began forming within the bounds of the central CS prior to reconnection  
 571        onset. Numerous X-points began forming and fully developed into plasmoids. Once on-  
 572        set was reached, the plasmoids had grown to be at least five times larger (in Z) than the  
 573        initial current sheet thickness.

- 574        • Frames a) and b) show that the current sheet is completely subdivided and bounded  
 575        by the plasmoids.
- 576        • Frame c) shows motion towards the current sheet both above and below. This mo-  
 577        tion is associated with each of the X-points
- 578        • Frame d) shows  $H^+$  motion away from the X-point. This motion is indicative of  
 579        outflow jets. The jets are five times larger in the z-direction than in Run 8 or the  
 580        baseline runs. The evolution of the bifurcated current sheet (not shown) is simi-  
 581        lar to that of Run 8 shown in Figure 6, except that it is divided by the multiple  
 582        X-lines.
- 583        • Frame e) shows that the evolution of the reconnection electric field is distinctly  
 584        different than Run 8 or the baseline runs. For Run 8 and the baselines, the two  
 585        points of localized  $E_y$  are on either side of the X-point along the x-axis. For Run  
 586        22 the two points of localized  $E_y$  are on either side of the X-point along the z-axis.  
 587        This is also seen in Run 21, Run 12, Run 13, and Run 23. In Run 11 there were  
 588        not two points of localized  $E_y$ ; instead it covered an area all around the X-point.
- 589        • Frame f) shows the development of one primary and multiple secondary quadrupole  
 590        out-of-plane magnetic structures.

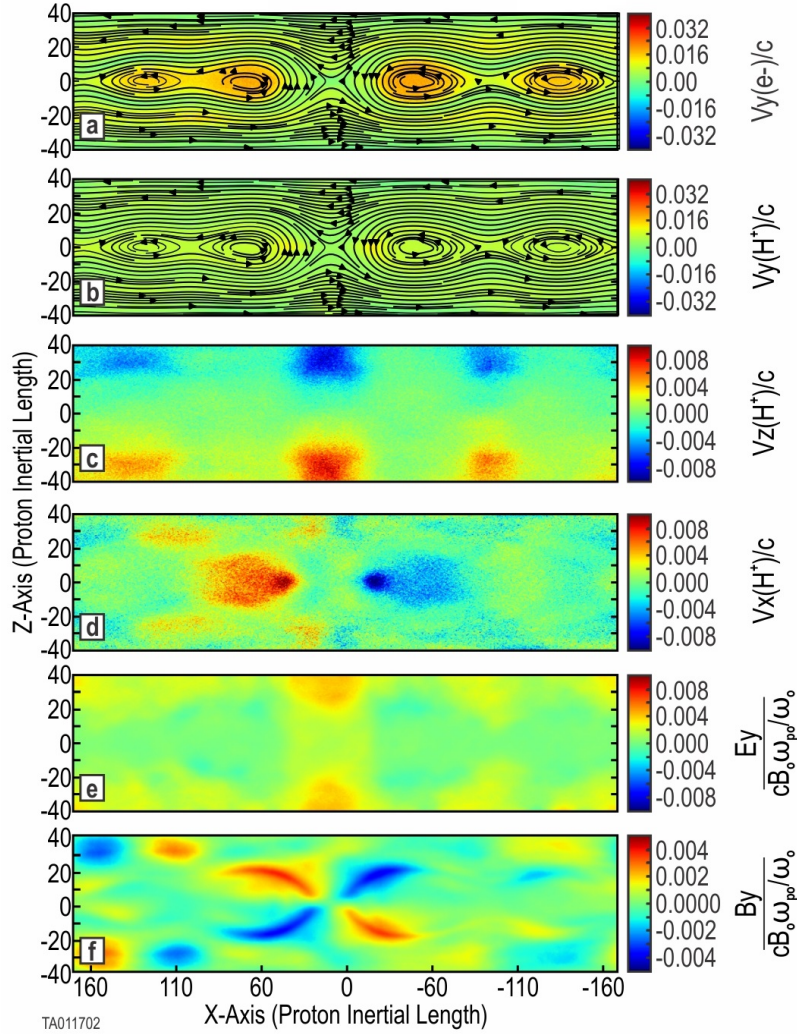


**Figure 5.** Key parameters for the 14.0 keV energized  $O^+$  simulation (Run 22). Shown are 2D color plots of key system parameters at 1,000 time steps ( $t=8194$ ) after onset of magnetic reconnection. Frames a) and b) are the  $v_y$  component of electron and proton current overlaid with the in-plane magnetic field lines. Frame c) shows the  $v_z$  component of the background protons. Frame d) shows the  $v_x$  component of the protons forming outlet jets. Frame e) gives the  $E_Y$  component of the electric field. Frame f) provides the  $B_y$  magnetic field.

- The 10.5 keV (Run 11 and Run 21) were just beginning to develop multiple X-points, but never fully developed into a plasmoid chain system during our simulations.
- The 14.0 keV (Run 12 and Run 22) simulations reached onset well before the previous three energies.
- The 17.5 keV (Run 13 and Run 23) simulations reached onset even sooner.

### 3.3.3 Reconnected Magnetic Flux

We investigated the reconnected magnetic flux to understand the state, rate and effectiveness of the reconnecting system evolution. We evaluated and compared the instantaneous flux,  $\Phi(t)$ , differential flux,  $\Delta\Phi(t)$ , and integral flux,  $\Sigma\Phi(t)$ . These were calculated according to section §2.5..

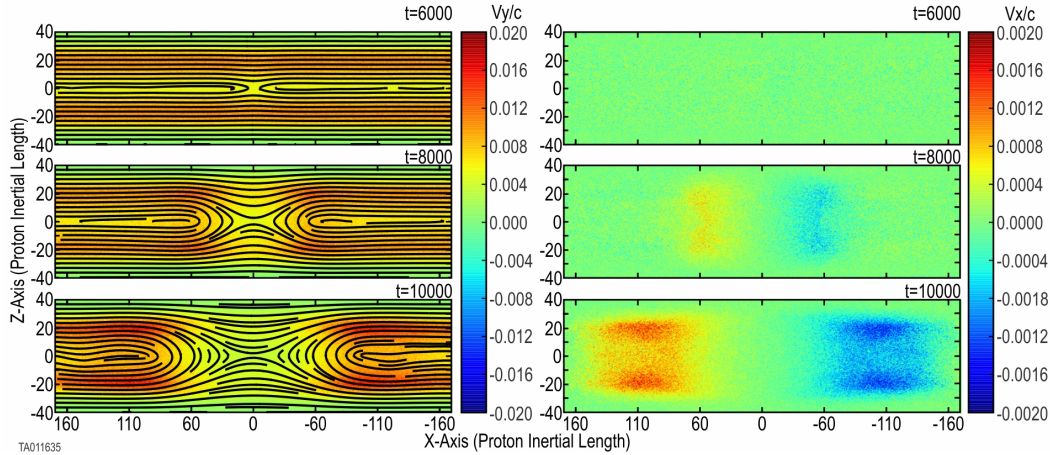


**Figure 6.** Time evolution of the onset of magnetic reconnection with a background of energized  $O^+$ . Shown, top to bottom, is Run 8 at three time-steps (6,000, 8,000, and 10,000). The left side shows the  $O^+$  velocity in the out-of-plane direction forming the duskward BCS overlaid with the in-plane magnetic field lines. The right side shows the  $O^+$  velocity in the X direction, Earthward or tailward. This indicates the bifurcated  $O^+$  turning into the outflow region forming bifurcated outflow jets.

602 Figure 7 shows plots of the instantaneous flux,  $\Phi(t)$ , plotted as a function of time.  
 603  $\Phi(t)$  allows comparisons, between runs, of the overall evolution of the system. The broken  
 604 red curves show the baseline simulations, Run 1 and Run 2 for reference. Run 1 and  
 605 Run 2 each show a peak then decrease of  $\Phi(t)$ . The decrease is due to secondary recon-  
 606 nection of the islands in the outflow region. These have the same relative behavior as  
 607 the two-species to three-species thermal comparisons found in Karimabadi et al. (2011),  
 608 Tenfjord et al. (2019), Markidis et al. (2011), and Liang et al. (2016). The thermal  $O^+$   
 609 in Run 2 caused a reduction (from no  $O^+$ ) in the peak amount of flux and the recon-  
 610 nection rate (slope). The solid black curves reveal the change in system response as en-  
 611 ergization increases. With 0.7 keV (Run 4) of energized  $O^+$ , the peak  $\Phi(t)$  and the re-  
 612 connection rate (slope) were reduced slightly more than thermal  $O^+$ . This is not unex-  
 613 pected, since this level of energization is only slightly higher than the thermal energy.  
 614 Each subsequent increase in energization further decreases the reconnection rate and peak  
 615  $\Phi(t)$ . Run 11 sees an increase in in both rate and peak. Although not within our simu-  
 616 lation time frame, Run 11 would have likely experienced a peak as the slower-forming  
 617 plasmoids eventually coalesced. The broken green curves show a comparison of the dif-  
 618 ference in the general evolution for increasing levels of energization. Run 12 and Run  
 619 13 see an increasingly higher reconnection rate and peak  $\Phi(t)$ . Run 12 and Run 13 also  
 620 show a peak then decrease of  $\Phi(t)$ . This decrease is due to secondary reconnection of the  
 621 plasmoid chain.

622 While  $\Phi(t)$  can increase or decrease depending on the occurrence of primary or sec-  
 623 ondary reconnection,  $\Sigma\Phi(t)$  continuously increases over the system evolution.  $\Sigma\Phi(t)$  is  
 624 an indication of the overall effectiveness of the reconnection engine.

625 Figure 8 shows  $\Sigma\Phi(t)$ , the integrated flux, plotted as a function of time for each  
 626 energization. This figure shows how the  $\Sigma\Phi(t)$ , and thus the overall effectiveness of the  
 627 system, decreases with each increase for the lower energizations, then reverses and be-  
 628 comes more effective at the two highest energizations.

629 To better analyze the variation in the reconnection rate, we calculated the differ-  
 630 ential flux,  $\Delta\Phi(t)$  for each energization. Values at 1,000 time steps after onset are shown  
 631 in Figure 9 (green triangle markers) using the right-hand scale. As the energization in-

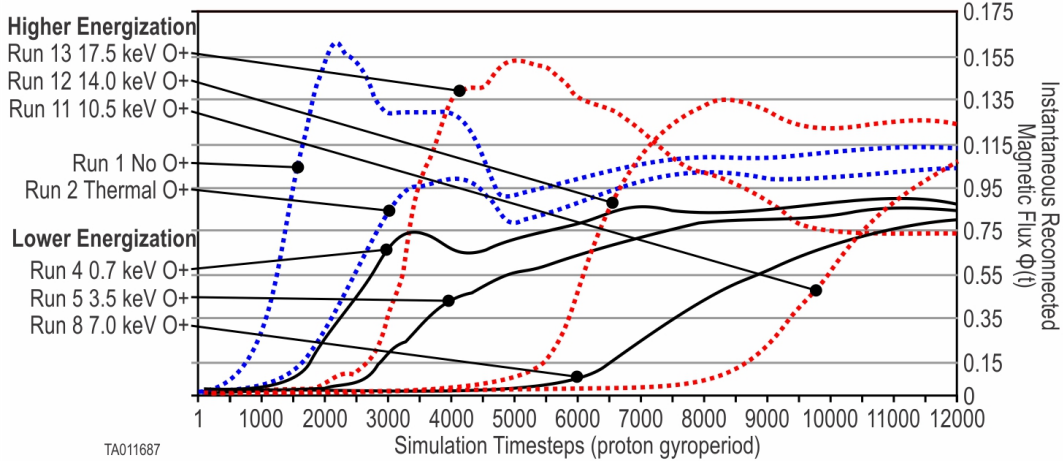


**Figure 7.** Instantaneous reconnected magnetic flux  $\Phi(t)$  : Taken from simulation time step  $t=0$ . Time plots of the instantaneous reconnected magnetic flux,  $\Phi(t)$ . The broken red lines indicate two baseline simulations (Run 1 and Run 2). The three solid black lines indicate the lower-regime simulations (Run 4, Run 5, and Run 8). The broken green lines indicate the higher-regime simulations (Run 11, Run 12, and Run 13). The associated energization is indicated for each run.  $\Phi(t)$  indicates the state of the system at a given time. Increasing amounts of  $\Phi(t)$  indicate reconnection with the  $B_x$  magnetic field components converting into  $B_z$  components. Similarly, decreasing amounts of  $\Phi(t)$  indicate secondary reconnection with the  $B_z$  magnetic field components converting into  $B_x$ . This is indicative of coalescing of adjacent O-points or plasmoids. Note that not all runs are shown in this plot.

632 creases at lower levels, the reconnection rate decreases. As the energization increases fur-  
 633 ther, this trend reverses and the reconnection rate starts to increase.

### 634 3.3.4 Time-to-Onset of Magnetic Reconnection

635 For a second comparison, we analyzed the time-to-onset of magnetic reconnection.  
 636 Here we found that  $O^+$  has a major impact. Each simulation was initiated at time step  
 637 zero with the same central current sheet thickness and same initial current profile. We  
 638 ran ten simulations (Run 4 through Run 13) with ten values of  $O^+$  energization to cover  
 639 the parameter space. Additionally, we ran ten identical simulations (Run 14 through Run  
 640 23) using a larger simulation box. We determined the time-to-onset for each of these us-  
 641 ing the method in §2.5. These results are tabulated in Table 1 and plotted in Figure 9.  
 642 Figure 9 shows the time-to-onset for the small simulation box runs (blue markers). As  
 643 energization increases over the lower values, time-to-onset increases. When energization  
 644 increases further an equally distinctive decrease is seen. Figure 9 also shows the time-  
 645 to-onset for the large box simulations (orange markers). The same trends are observed  
 646 in the larger simulation box, however the trend reversal occurs at a lower energization.  
 647 Also, the time-to-onset is systematically longer in the larger box. These differences are  
 648 discussed in §4.2; which addresses the simulation box size.

### 649 3.4 $O^+$ Density and CS Thickness

650 Two simulations with lower  $O^+$  density were performed at two energizations. Three  
 651 simulations, with a thicker or thinner CS were also performed at these two energizations.

652 Run 8 and Run 12 each had an  $O^+$  density of  $0.1 n_o$ . These were repeated with  
 653 an  $O^+$  density of  $0.05 n_o$  in Run 24 and Run 25, respectively. Run 8 reached onset at  
 654 6,207 time steps, while Run 24 reached onset at 1,783 time steps. Run 12 reached on-

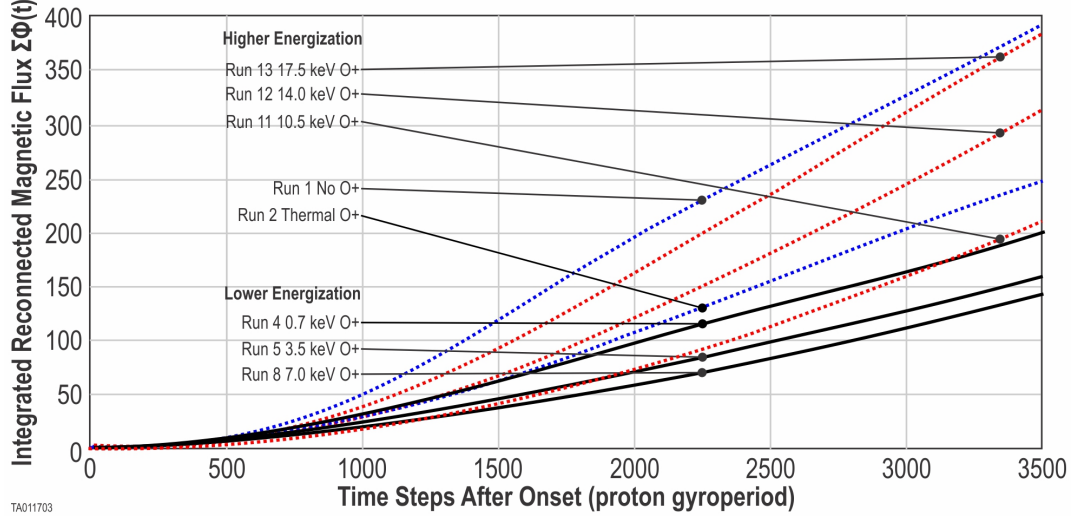


**Figure 8.** Integrated reconnected magnetic flux  $\Delta\Phi(t)$  : Time is zeroed to start at the time of onset for each run. Run 1 is a baseline with no  $O^+$ , Run 2 is a baseline with thermal  $O^+$ , Run 4 has energized  $O^+$  0.7 keV, Run 5 has energized  $O^+$  3.5 keV, Run 7 has energized  $O^+$  7.0 keV, Run 9 has energized  $O^+$  10.5 keV, Run 10 has energized  $O^+$  14.0 keV, Run 11 has energized  $O^+$  17.5 keV. Note that not all runs are shown in this plot.

655 set at 5,162 time steps, while Run 25 reached onset at 3,311 time steps. Run 12 reached  
 656 onset with multiple X-lines, while the lower-density Run 25 reached onset with a single  
 657 primary X-line.

658 Run 8 at 7.0 keV was replicated with a thicker and thinner CS in Run 26 and Run  
 659 28, respectively. While Run 8 reached onset at 6,207 time steps, Run 26 with a CS thick-  
 660 ness of 3.0 had not reached onset after 25,000 time steps. Run 28 reached onset at 1,860  
 661 time steps, well before Run 8. Run 12 at 14.0 keV was replicated with a thicker CS in  
 662 Run 27. Run 27 reached onset at 5,600 time steps, nearly the same as Run 12 at 5,162  
 663 time steps.

### 664 3.5 Background $H^+$

665 An important aspect of the simulations is the different behavior of the  $H^+$  back-  
 666 ground between the runs with and without energized  $O^+$ . All of the simulations started  
 667 with an initial background population of thermal  $H^+$  equal to  $0.1 n_o$ . In all three base-  
 668 line simulations without energized  $O^+$ , this density remained constant at  $0.1 n_o$  until re-  
 669 connection onset. At that time the background changed as it became involved in the re-  
 670 connection inflow, as expected. In contrast, during all of the runs with energized  $O^+$ ,  
 671 the background  $H^+$  did not remain constant. As time progressed, the  $H^+$  background  
 672 was depleted near the CS and enhanced away from the CS. Figure 10 shows a time se-  
 673 quence of this depletion, which is typical of all of the energized  $O^+$  cases. With ener-  
 674 gized  $O^+$  present, the initial  $H^+$  density of  $0.1 n_o$  (black) immediately begins to deplete  
 675 (green) near the central CS. There is also an increase in the  $H^+$  density above the ini-  
 676 tial value at about  $\pm 30$  proton inertial lengths away. Just prior to onset the density  
 677 around the central CS has depleted even further (red). The corresponding increase in  
 678 the peaks at  $\pm 30$  proton inertial lengths are even greater. This depletion became more  
 679 pronounced as the  $O^+$  energization increased. We observed a difference in the depletion  
 680 between simulations performed in the larger box and the smaller box, which is discussed  
 681 in §4.2.

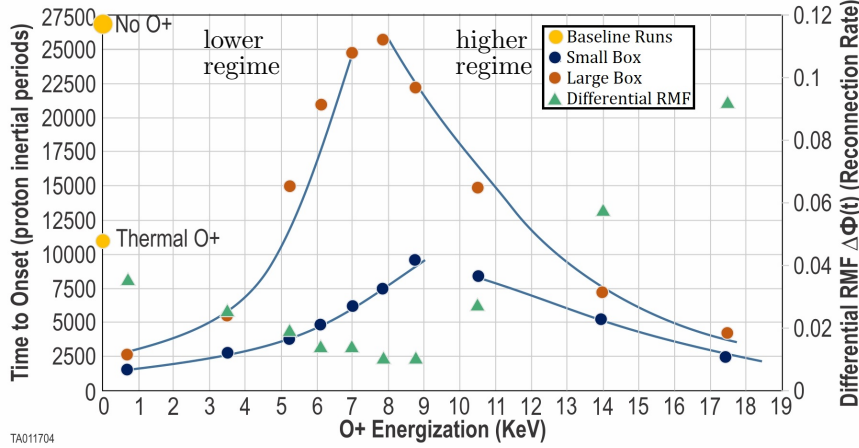


**Figure 9.** This figure depicts the lower and higher onset regimes for energized  $O^+$ . The blue markers show the time-to-onset for the ten  $O^+$  energizations in the small simulation boxes. The orange markers show the time-to-onset for the ten  $O^+$  energizations in the large simulation boxes. The green markers show the differential flux for the ten  $O^+$  energizations in the small simulation boxes. For reference, we include the labeled yellow markers show the differential flux for the no  $O^+$  and thermal  $O^+$  runs. Differences in the time-to-onset and the point where the regime changes are discussed in §4.2.

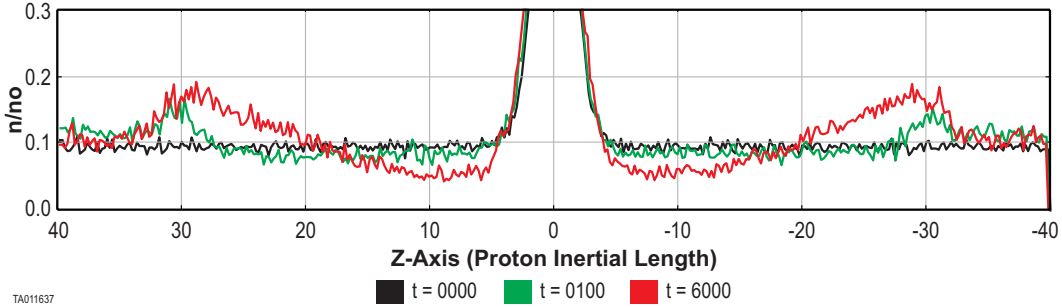


**Figure 10.** A time sequence plot of the  $H^+$  density in Run 8 at three points leading up to onset. The peaks are cut off only to emphasize the background population.

## 682 4 Discussion

### 683 4.1 Two-Regime Onset

684 In our simulations of a thinning current sheet, we see two distinct, system-level re-  
 685 sponse types to the onset of magnetic reconnection. These two response types manifest  
 686 themselves in several ways: through differences in topology, the reconnected magnetic  
 687 flux parameters (§2.5) and the time-to-onset. In otherwise identical simulations, these  
 688 responses varied according to the energization of a background population of  $O^+$ . Since  
 689 these responses occur at either lower and higher  $O^+$  energization, we refer to them sim-  
 690 ply as the lower-regime and the higher-regime.

#### 691 4.1.1 Lower-Regime

692 System responses in the lower-regime follow a systematic evolution that is a func-  
 693 tion of increasing  $O^+$  energization. In the lower-regime:

- 694 • Magnetic reconnection onsets via a tearing instability.
- 695 • The system forms a single primary X-line.
- 696 • As energization increases:
- 697 – The peak instantaneous reconnected flux decreases.
- 698 – The differential (reconnection rate) reconnected flux decreases.
- 699 – The integrated reconnected flux decreases.
- 700 – The time-to-onset increases.

701 Given that CS thinning leads to the onset of magnetic reconnection, anything that  
 702 alters this thinning must affect time-to-onset. A general mechanism for CS thinning in  
 703 the magnetotail is the external lobe pressure applied to the central CS of the plasma sheet.  
 704 This produces an imbalance of the external pressure to the internal pressure within the  
 705 central CS. When the external pressure exceeds the pressure internal to the CS, the im-  
 706 balance causes thinning of the CS, leading ultimately to onset of magnetic reconnection.  
 707 It follows that a lessening of this external pressure would produce a reduction of the thin-  
 708 ning. This in turn would produce a delay in reaching the onset of magnetic reconnec-  
 709 tion.

710 Our results indirectly show a difference in this external pressure between simula-  
 711 tions with and without energized  $O^+$ . Since the  $H^+$  background around the central CS  
 712 is and remains thermal, its pressure is directly proportional to its density ( $p = nk_B T$ ).  
 713 All of our simulations were initialized with a thermal  $H^+$  background density of  $0.1 n_o$ .  
 714 For Run 1 (no  $O^+$ ), Run 2, and Run 3 (both thermal  $O^+$ ), this background  $H^+$  den-  
 715 sity remained uniform at  $0.1 n_o$ . It remained so until onset, when the magnetic recon-  
 716 nection process began moving the background  $H^+$  ions away from the CS. This move-  
 717 ment produced a distinct depletion around the CS and enhancement away from the CS  
 718 (Figure 10). This depletion and enhancement occurred for all runs with energized  $O^+$ .

719 Although the mechanism was not identified as part of this study, it is most certainly  
 720 a direct result of the  $O^+$  energization. This depletion around the central CS directly re-  
 721 duces the external to internal pressure gradient between surrounding  $H^+$  and the cen-  
 722 tral CS. This in turn slows the CS thinning, which ultimately delays of the onset of mag-  
 723 netic reconnection.

#### 724 **4.1.2 Higher-Regime**

725 System response in the higher-regime follows a systematic evolution, which is a func-  
 726 tion of increasing  $O^+$  energization. In the higher-regime:

- 727 • Magnetic reconnection onsets via a secondary tearing (plasmoid) instability.
- 728 • The system forms multiple X-lines.
- 729 • As energization increases above a critical transition.
- 730 – The peak instantaneous reconnected flux increases.
- 731 – The differential (reconnection rate) reconnected flux increases.
- 732 – The integrated reconnected flux increases.
- 733 – The time-to-onset decreases.
- 734 – The number of plasmoids increases.

735 Transitioning from the lower to higher-regime is evidenced by a major change in  
 736 the reconnection topology, specifically, changing from a single primary X-line to multi-  
 737 ple X-lines. The mechanism causing this transition is correlated with the presence of en-  
 738 ergized  $O^+$ . In the lower-regime, the  $O^+$  caused the  $H^+$  to move away and slow the CS  
 739 thinning. At the transition point between both regimes,  $O^+$  continues to affect the  $H^+$ ,

740 moving it away from the CS. In fact, the higher the energization, the more effect it has  
 741 on the background  $H^+$ . Examination of the  $H^+$  depletion indicates that the effects in  
 742 the higher-regime occur as a result of this depletion.

743 In the lower-regime,  $O^+$  moves the  $H^+$  away from the vicinity of the central CS.  
 744 In the higher-regime, the  $H^+$  depletion is more pronounced. This continues the corre-  
 745 lation between increased  $O^+$  energization and increased depletion seen in the lower-regime.  
 746 This enhanced depletion causes a higher internal to external pressure gradient. Near the  
 747 transition point between regimes, the depletion of  $H^+$  not only slows and stops the CS  
 748 thinning, it reverses it, and the CS begins to broaden. It broadens so much that the par-  
 749 ticle and current density in the central CS begins to diminish. The out-of-plane current  
 750 peak in the central CS also begins to diminish as it broadens. In comparison, this is ev-  
 751 ident by the color bar values (intensity) of Figure 5 a) and 5 b) being half of those of Fig-  
 752 ure 4 a) and 4 b). As the CS broadens to approximately twice the original thickness, mul-  
 753 tiple X-lines form within its bounds. This is referred to as a secondary tearing or plas-  
 754 moid instability. There is no magnetic reconnection taking place as evidenced by the lack  
 755 of a reconnection electric field or a quadrupole magnetic field. The amount of reconnected  
 756 magnetic flux remains low and fluctuates. Once the point of onset of magnetic recon-  
 757 nection is reached, as determined by  $\Phi(t)$ , the plasmoid size exceeds the original CS thick-  
 758 ness (Figure 5). Secondary reconnection begins, and the plasmoids eventually coalesce.

759 In addition to the diminishing content of the central CS, there could be an addi-  
 760 tional disruption mechanism caused by the Speiser-orbiting  $O^+$ . As the  $O^+$  has an ef-  
 761 fect on the background  $H^+$ , it could also have an effect on the CS. The scope of this work  
 762 did not include investigating such a mechanism.

763 In Figure 8, the  $\Sigma\Phi(t)$  curve at 10.5 keV (Run 11) crosses the curve at 3.5 keV  
 764 (Run 5) at  $\sim 1,700$  time steps and the curve of 0.7 keV (Run 8) at  $\sim 3,100$  time steps.  
 765 Looking at the topology of Run 11 over time (not shown), this run commences with two  
 766 primary X-lines and a third, not fully formed, X-line. This third X-line fully develops  
 767 shortly after onset, increasing the reconnection rate  $\Delta\Phi(t)$  and boosting  $\Sigma\Phi(t)$ .

768 Examination of  $O^+$  density in §3.4 indicates that less  $O^+$  reduces the  $H^+$  deple-  
 769 tion, the CS thinning and the time to reconnection onset. While not an exhaustive com-  
 770 parison, these two additional runs indicate that a decrease in number density produces  
 771 a lesser effect. Note that Run 10 with 14.0 keV resulted in a faster onset time due to a  
 772 different mode of instability disrupting the CS. Run 21, also with 14.0 keV but with 0.05  
 773  $n_o$   $O^+$  density, formed a single X-point, indicating that the resistive tearing mode be-  
 774 came dominant.

775 Results in §3.4 indicate that the CS thinning and time to reconnection onset is de-  
 776 pendent on initial CS thickness. A thicker CS, on the other hand, did not reach onset  
 777 even after 25,000 proton gyroperiods.

778 Figure 5 shows that the reconnection electric field,  $E_y$ , in Run 20 is distinctly dif-  
 779 ferent than what is seen in the lower-regime or baseline runs. We expect that there are  
 780 two points of localized  $E_y$  on either side of the X-point along the x-axis. For Run 22 the  
 781 two points of localized  $E_y$  are on either side of the X-point the z-axis. This variation in  
 782 reconnection electric field location is seen in four out of six higher-regime simulations.  
 783 This is possibly due to the depletion of the  $H^+$ , which may form Hall currents moving  
 784 in a non-traditional inflow region towards the X-point. A non-traditional inflow region  
 785 refers to that seen in Figure 4 c). It also may be caused by the two center plasmoids be-  
 786 ginning to coalesce. In either case, it is beyond the scope of this present investigation  
 787 and will require further study.

788 There is a critical  $O^+$  energization at which the system transitions from the lower-  
 789 regime to the higher-regime. In our simulations this occurs between 8.75 keV and 10.5

790 keV in the small box and between 7.0 keV and 7.875 keV in the large box. Why this hap-  
 791 pens is a result of simulation box size and is discussed in §4.2.

792 This regime change is suggestive of a collisionless plasma transitioning across  $\lambda_{crit}$   
 793 as depicted in a reconnection phase diagram (§1.2 and Ji and Daughton (2011)). The  
 794  $\lambda_{crit}$  separates regions where the onset of magnetic reconnection leads to a single X-point  
 795 or to multiple X-points in a plasmoid instability. This appears to be what is happening  
 796 in our system. However, the phase diagram referenced does not take into account effects  
 797 due to energized heavy ions. Uzdensky and Loureiro (2016) also present a two onset regimes:  
 798 one that produces a single-island and one that produces a multi-island system. These  
 799 two regimes are referred to as the Furth, Killeen and Rosenbluth (FKR) or the Ruther-  
 800 ford regime and the Coppi regime. Which regime is dominant is highly dependent on the  
 801 rate of current sheet formation. In recent years, the unlikelihood of a Sweet-Parker-like  
 802 current sheet forming due to background turbulence and the CS instability (Loureiro and  
 803 Uzdensky (2016) and references therein) has been discussed extensively. This does not  
 804 preclude a region of high Lundquist number,  $S$ , and low effective plasma size,  $\lambda$ , where  
 805 single X-point, collisionless, reconnection can take place (Ji & Daughton, 2011). Addi-  
 806 tionally, as is seen in published thermal  $O^+$  studies and our lower-regime,  $O^+$  can add  
 807 stability to the CS. This is especially possible considering the exclusion of thermal or en-  
 808 ergized  $O^+$  in any associated studies of plasmoid instability. There also have been no  
 809 investigations of the effect of energized  $O^+$  on the Lundquist number.

810 There is an interesting parallel in the similarity between our two-regime system with  
 811 energized  $O^+$  and those mentioned above. Our two-regime response is due to an inde-  
 812 pendently controllable variable applied to an otherwise invariant system. This provides  
 813 an in-depth method to study what causes a system, stable to a single X-line, to tran-  
 814 sition to one that develops a plasmoid chain.

## 815 4.2 Simulation Size

816 Two anomalies were seen when comparing the small and large simulations. First,  
 817 the time-to-onset values were systematically larger in the large simulation box. Second,  
 818 the point at which the larger box transitioned from lower-regime to higher-regime was  
 819 at a lower energization than the smaller box. Examination of the background  $H^+$  for  
 820 each box at each energization reveals the source of these differences. Based on this ex-  
 821 amination, we show that the physics simulated in the small box remains valid even though  
 822 there are small Z-boundary interactions.

823 The original box size for this study was selected to ensure that energized  $O^+$ , in  
 824 Speiser orbits, would not interact with the boundaries of the simulation. We previously  
 825 showed that a sustained  $O^+$  BCS can be simulated in the original box without experi-  
 826 encing boundary interactions (George & Jahn, 2020). This box was computationally 800  
 827 x 400 grid cells (X-dimension x Z-dimension) and physically 320 x 80 proton inertial lengths.  
 828 During the course of the investigation we found that there was a small, but quantifiable,  
 829 boundary interaction. When the energized  $O^+$  displaced the background  $H^+$ , the dis-  
 830 placement extended beyond the +/-Z range of the  $O^+$  and into the +/-Z boundaries.  
 831 Due to this interaction, we enlarged the box and re-performed the simulations. For these,  
 832 we doubled the size of the box in the Z-dimension. This resulted in a larger box that was  
 833 computationally 800 x 800 grid cells and physically 320 x 160 proton inertial lengths.

834 Since there was absolutely no boundary interaction with Run 1, we did not re-perform  
 835 it in the larger box. Since the thermal  $O^+$  was used to baseline the energized runs, Run  
 836 2 (thermal  $O^+$ ) was replicated in the larger box in Run 3. Both reached reconnection  
 837 onset at essentially the same time, 1,422 and 1,474 time steps, respectively. Each evolved  
 838 in a nearly identical manner after reaching onset, which indicates that there was no in-  
 839 teraction due Z boundaries in the smaller box.

840 For the energized  $O^+$  runs in the smaller box, we noted a small, but quantifiable  
 841 boundary interaction that warrants discussion. To address and determine the extent of  
 842 the interaction on our results we reran these simulations using a larger box (320 x 160).

843 The same energized  $O^+$  populations were used in these simulations and, again, had  
 844 no boundary interaction. As discussed above, the Speiser-orbiting energized  $O^+$  caused  
 845 a depletion region to form in the background  $H^+$  around the central CS. While depletion  
 846 occurred near the central CS, peaks were formed at the edge of the bifurcated cur-  
 847 rent sheet with the displaced  $H^+$ . Figure 11 shows that the locations of the peaks around  
 848 the BCS differ slightly between otherwise identical simulations in the small and large box.  
 849 For Run 8 (smaller box) these peaks occurred at about  $\pm 30$  proton inertial lengths.  
 850 For Run 18 in the larger box these peaks occurred at about  $\pm 38$  proton inertial lengths.  
 851 Except for the simulation box size, each set of ten simulations were otherwise identical.  
 852 Each of the ten runs with varying energization was replicated in a larger simulation box.  
 853 In each case the time-to-onset was greater in the larger box (Figure 9). In each case, an  
 854 examination of the  $H^+$  density depletion around the central CS reveals the source of this  
 interaction. The boundary of the smaller box actually prevented the background  $H^+$  from

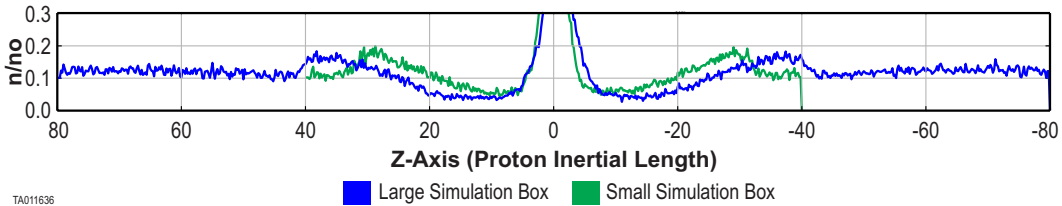


**Figure 11.** Z-Cut of  $H^+$  density at the center of the simulation box, just before onset, for Run 8 (small simulation box - green) and Run 18 (large simulation box - blue). Both are taken at  $t=6,000$  time steps. This shows that the Z boundary at  $\pm 40$  lessened the  $H^+$  depletion (green) around the central CS when compared to that in the larger simulation. The larger box allows for  $H^+$  depletion to extend a few gyro-radii further. This lowers the density immediately around the central CS, reducing the thinning and further delaying the offset.

855 moving further out. This is due to the plasma back-pressure against the specularly re-  
 856 flecting Z boundary. Once the box was enlarged, this back-pressure no longer hindered  
 857 the outward movement of the background  $H^+$ . This allowed the background around the  
 858 central CS to deplete an additional amount, which further reduced the external pressure  
 859 on the central CS. This slight reduction was enough to further slow the thinning and ex-  
 860 tend the time-to-onset. This explains the increased time-to-onset as the energization in-  
 861 creased. It also explains why the system transitioned from the lower-regime to the higher-  
 862 regime. Very simply, between the larger box and the smaller box, Figure 11 shows that  
 863 the  $H^+$  needed just a little more room to be pushed out just a little bit farther. Prevent-  
 864 ing the  $H^+$  from being pushed out that small amount was enough to increase the den-  
 865 sity around the central CS; producing enough pressure to thin the CS, which initiated  
 866 onset sooner in the smaller box. In the larger box it is evident that the additional den-  
 867 sity reduction slows the CS thinning even more, producing a much greater onset delay.  
 868 From these comparisons of the large to small simulations, we can conclude that even though  
 869 the smaller box did affect the quantitative results, qualitatively the physics (of the back-  
 870 ground  $H^+$  depletion and the CS disruption) is the same in the smaller box.  
 871

## 872 5 Summary and Conclusion

873 The study of  $O^+$  in reconnection simulations has been limited to a background of  
 874 thermal ions. Published results demonstrate that the effects of thermal  $O^+$  on magnetic  
 875 reconnection are minor. Thermal  $O^+$  essentially behaves like heavier protons. To study

876 the effect of energized  $O^+$  on the magnetic reconnection process, we first baselined our  
 877 simulation setup, repeating published simulations with a background of either thermal  
 878  $H^+$  or thermal  $O^+$ . Our results mirrored those of published results, indicating a valid  
 879 setup.

880 Since energized  $O^+$  has been observed in conjunction with current sheets and mag-  
 881 netic reconnection, it should be examined in simulation studies. We introduced a pop-  
 882 ulation of energized  $O^+$  into our baseline simulations of a thinning current sheet. We  
 883 ran 25 simulations with variations in  $O^+$  energization, density, and CS thicknesses. We  
 884 analyzed the evolution and onset of each system by comparing key parameters of each  
 885 simulation. These included the current sheet structure, the inflow and outflow region struc-  
 886 ture, and the out-of-plane electric and magnetic field formation. We studied the effects  
 887 of energized  $O^+$  by analyzing the instantaneous, differential, and integral flux (§3.3.3).  
 888 This provided information about the state of each system, the rate at which it evolved,  
 889 and its overall effectiveness as a reconnection engine. Finally, we determined the time-  
 890 to-onset of magnetic reconnection (§3.3.4) at the various energizations. From these re-  
 891 sults, we can conclude that:

- 892 • Energized  $O^+$  has a major impact on the onset and evolution of magnetic recon-  
 893 nection.
- 894 • The presence of energized  $O^+$  causes a two-regime onset response in a thinning  
 895 current sheet.
- 896 • At lower energization,  $O^+$  increases time-to-onset and suppresses the rate of evo-  
 897 lution.
- 898 • At higher energization,  $O^+$  decreases time-to-onset and enhances the rate of evo-  
 899 lution.

900 Our results show that, unlike thermal  $O^+$ , energized  $O^+$  populations do have a ma-  
 901 jor impact on the onset and evolution of magnetic reconnection. Changes in both the  
 902 energization and number density of the  $O^+$  contribute to its impact. Over the energy  
 903 range we studied, we found that energized  $O^+$  leads to a dual-regime response of these  
 904 parameters. These regimes are based on  $O^+$  energization, and are referred to as the "lower-  
 905 regime" and the "higher-regime".

906 In the lower-regime, the time-to-onset of reconnection increases with  $O^+$  energiza-  
 907 tion, while the amount of reconnected flux and reconnection rate decrease. Similarly in  
 908 the higher-regime, the time-to-onset of reconnection decreases with  $O^+$  energization, while  
 909 the amount of reconnected flux and the reconnection rate increase.

910 The topologies in these two regimes show that magnetic reconnection proceeds ac-  
 911 cording to two different mechanisms. Although their evolution is quite different, they  
 912 both appear to be a result of tearing instabilities in the current sheet. In the lower-regime,  
 913 reconnection occurs via a simple tearing instability at a single primary X-point. In the  
 914 higher-regime, reconnection occurs at multiple X-points, forming a stochastic plasmoid  
 915 chain.

916 Closer examination of the evolution of both the lower and higher-regimes shows  
 917 the mechanism that causes the behavior. The Speiser-orbiting  $O^+$  depletes the background  
 918  $H^+$  bordering the central CS. This  $H^+$  depletion around the central CS lowers the ex-  
 919 ternal pressure responsible for thinning the CS. The lower pressure slows CS thinning,  
 920 leading to an increase in time-to-onset of magnetic reconnection. This effect is more pro-  
 921 nounced as the  $O^+$  energization increases. Once onset occurs, depletion of  $H^+$  around  
 922 the current sheet also starves the reconnection process of inflow material, slowing the  
 923 evolution of reconnection itself.

924 In the higher-regime, the same depletion drives the behavior. As  $O^+$  energization  
 925 increases in the lower-regime, it revealed that the CS thinning slowed. When energiza-

tion reaches and exceeds a critical value, the CS not only stops thinning, but the process actually reverses, and the CS begins to broaden. It broadens enough that the particle and current density in the CS begin to diminish. This eventually disrupts the CS via an extensive tearing instability, referred to as a secondary tearing or plasmoid instability. This effect is more pronounced as the  $O^+$  energization increases, thus decreasing the time-to-onset. The creation and growth of multiple plasmoids facilitates numerous X-points, driving the amount and rate of reconnected flux higher.

The two-regime nature of the impact of energized  $O^+$  on tail-like reconnection is a robust result over the parameter space considered. Future steps could include the study of energized  $O^+$  in 3D, and the inclusion of a physics-based acceleration mechanism of  $O^+$  energization rather than an ad-hoc seeding of the energized  $O^+$  population. Nevertheless, the behavior and contribution of energized  $O^+$  upon magnetic reconnection needs to be investigated in more detail to come to a full understanding of reconnecting systems under the influence of  $O^+$ .

## Acknowledgments

Follow this link: [https://zenodo.org/record/3593343#.Xiu\\_82hKi70](https://zenodo.org/record/3593343#.Xiu_82hKi70) for the simulation code used in this study.

Research at Southwest Research Institute was funded in part by NASA through the MMS prime contract NNG04EB99C.

The authors thank Micheal Hesse and NASA Goddard Space Flight Center for providing the Particle-In-Cell code used in this work as well as instruction in its use.

## References

- Baker, D. N., Hones, J., E. W., Young, D. T., & Birn, J. (1982, Dec). The possible role of ionospheric oxygen in the initiation and development of plasma sheet instabilities. *Geophysical Research Letters*, *9*(12), 1337-1340. doi: 10.1029/GL009i012p01337
- Birn, J., Drake, J. F., Shay, M. A., Rogers, B. N., Denton, R. E., Hesse, M., ... Pritchett, P. L. (2001, March). Geospace environmental modeling (gem) magnetic reconnection challenge. *Journal of Geophysical Research*, *106*(A3), 3715-3720. doi: 10.1029/1999JA900449
- Birn, J., & Hesse, M. (1994, January). Particle acceleration in the dynamic magnetotail: Orbits in self-consistent three-dimensional mhd fields. *Journal of Geophysical Research (Space Physics)*, *99*(A1), 109-120. doi: 10.1029/93JA02284
- Birn, J., & Hesse, M. (2001, Mar). Geospace Environment Modeling (GEM) magnetic reconnection challenge: Resistive tearing, anisotropic pressure and hall effects. *Journal of Geophysical Research*, *106*(A3), 3737-3750. doi: 10.1029/1999JA001001
- Birn, J., Thomsen, M., & Hesse, M. (2004, April). Acceleration of oxygen ions in the dynamic magnetotail. *Annales Geophysicae*, *22*(4), 1305-1315. doi: 10.5194/angeo-22-1305-2004
- Comisso, L., & Bhattacharjee, A. (2016, December). On the value of the reconnection rate. *Journal of Plasma Physics*, *82*(6), 595820601. doi: 10.1017/S002237781600101X
- Daughton, W., Roytershteyn, V., Albright, B. J., Karimabadi, H., Yin, L., & Bowers, K. J. (2009, August). Transition from collisional to kinetic regimes in large-scale reconnection layers. *Physical Review Letters*, *103*(6), 065004. doi: 10.1103/PhysRevLett.103.065004
- Daughton, W., Scudder, J., & Karimabadi, H. (2006, Jul). Fully kinetic simulations of undriven magnetic reconnection with open boundary conditions. *Physics of*

- 975 *Plasmas*, 13(7), 072101. doi: 10.1063/1.2218817
- 976 George, D. E., & Jahn, J.-M. (2020, February). Energized Oxygen in the Magne-  
977 totail: Current Sheet Bifurcation From Speiser Motion. *Journal of Geophysical*  
978 *Research (Space Physics)*, 125(2), e27339. doi: 10.1029/2019JA027339
- 979 Harris, E. G. (1962, January). On a plasma sheath separating regions of oppo-  
980 sately directed magnetic field. *Il Nuovo Cimento*, 23, 115-121. doi: 10.1007/  
981 BF02733547
- 982 Hesse, M., & Birn, J. (2004, February). On the cessation of magnetic reconnection.  
983 *Annales Geophysicae*, 22, 603-612. doi: 10.5194/angeo-22-603-2004
- 984 Hesse, M., Birn, J., & Kuznetsova, M. (2001, March). Collisionless magnetic re-  
985 connection: Electron processes and transport modeling. *Journal of Geophysical*  
986 *Research (Space Physics)*, 106, 3721-3736. doi: 10.1029/1999JA001002
- 987 Hesse, M., & Schindler, K. (2001, June). The onset of magnetic reconnec-  
988 tion in the magnetotail. *Earth, Planets, and Space*, 53, 645-653. doi:  
989 10.1186/BF03353284
- 990 Hesse, M., Schindler, K., Birn, J., & Kuznetsova, M. (1999, May). The diffusion re-  
991 gion in collisionless magnetic reconnection. *Physics of Plasmas*, 6, 1781-1795.  
992 doi: 10.1063/1.873436
- 993 Ipavich, F. M., Galvin, A. B., Gloeckler, G., Hovestadt, D., Klecker, B., & Sc-  
994 holer, M. (1984, May). Energetic (greater than 100 keV) o(+) ions  
995 in the plasma sheet. *Geophysics Research Letters*, 11, 504-507. doi:  
996 10.1029/GL011i005p00504
- 997 Ji, H., & Daughton, W. (2011, November). Phase diagram for magnetic reconnec-  
998 tion in heliophysical, astrophysical, and laboratory plasmas. *Physics of Plas-*  
999 *mas*, 18(11), 111207-111207. doi: 10.1063/1.3647505
- 1000 Karimabadi, H., Roytershteyn, V., Mouikis, C. G., Kistler, L. M., & Daughton,  
1001 W. (2011, May). Flushing effect in reconnection: Effects of minority  
1002 species of oxygen ions. *Planetary and Space Science*, 59, 526-536. doi:  
1003 10.1016/j.pss.2010.07.014
- 1004 Kistler, L. M., Mouikis, C., MøBius, E., Klecker, B., Sauvaud, J. A., RéMe, H., ...  
1005 Balogh, A. (2005, June). Contribution of nonadiabatic ions to the cross-  
1006 tail current in an o<sup>+</sup> dominated thin current sheet. *Journal of Geophysical*  
1007 *Research (Space Physics)*, 110, A06213. doi: 10.1029/2004JA010653
- 1008 Kronberg, E. A., Ashour-Abdalla, M., Dandouras, I., Delcourt, D. C., Grig-  
1009 orenko, E. E., Kistler, L. M., ... Zelenyi, L. M. (2014, November). Circu-  
1010 lation of heavy ions and their dynamical effects in the magnetosphere: Re-  
1011 cent observations and models. *Space Science Review*, 184, 173-235. doi:  
1012 10.1007/s11214-014-0104-0
- 1013 Liang, H., Ashour-Abdalla, M., Lapenta, G., & Walker, R. J. (2016, Feb). Oxygen  
1014 impacts on dipolarization fronts and reconnection rate. *Journal of Geophysical*  
1015 *Research (Space Physics)*, 121(2), 1148-1166. doi: 10.1002/2015JA021747
- 1016 Liang, H., Lapenta, G., Walker, R. J., Schriver, D., El-Alaoui, M., & Berchem,  
1017 J. (2017, Jan). Oxygen acceleration in magnetotail reconnection. *Jour-*  
1018 *nal of Geophysical Research (Space Physics)*, 122(1), 618-639. doi: 10.1002/  
1019 2016JA023060
- 1020 Liu, Y., Kistler, L. M., Mouikis, C. G., Klecker, B., & Dandouras, I. (2013, May).  
1021 Heavy ion effects on substorm loading and unloading in the Earth's magne-  
1022 totail. *Journal of Geophysical Research (Space Physics)*, 118(5), 2101-2112. doi:  
1023 10.1002/jgra.50240
- 1024 Liu, Y. H., Mouikis, C. G., Kistler, L. M., Wang, S., Roytershteyn, V., &  
1025 Karimabadi, H. (2015). The heavy ion diffusion region in magnetic reconnec-  
1026 tion in the earth's magnetotail. *Journal of Geophysical Research: Space*  
1027 *Physics*, 120(5), 3535-3551. doi: 10.1002/2015JA020982
- 1028 Loureiro, N. F., Schekochihin, A. A., & Cowley, S. C. (2007, October). Instability of  
1029 current sheets and formation of plasmoid chains. *Physics of Plasmas*, 14(10),

- 100703-100703. doi: 10.1063/1.2783986
- 1030  
1031 Loureiro, N. F., & Uzdensky, D. A. (2016, January). Magnetic reconnection: from  
1032 the Sweet-Parker model to stochastic plasmoid chains. *Plasma Physics and  
1033 Controlled Fusion*, *58*(1), 014021. doi: 10.1088/0741-3335/58/1/014021
- 1034 Lyons, L. R., & Speiser, T. W. (1982, April). Evidence for current sheet acceleration  
1035 in the geomagnetic tail. *Journal of Geophysical Research*, *87*, 2276-2286. doi:  
1036 10.1029/JA087iA04p02276
- 1037 Markidis, S., Henri, P., Lapenta, G., Divin, A., Goldman, M. V., Newman, D.,  
1038 & Eriksson, S. (2012, February). Collisionless magnetic reconnection in a  
1039 plasmoid chain. *Nonlinear Processes in Geophysics*, *19*(1), 145-153. doi:  
1040 10.5194/npg-19-145-2012
- 1041 Markidis, S., Lapenta, G., Bettarini, L., Goldman, M., Newman, D., & Andersson,  
1042 L. (2011, September). Kinetic simulations of magnetic reconnection in pres-  
1043 ence of a background  $\text{o}^+$  population. *Journal of Geophysical Research (Space  
1044 Physics)*, *116*, A00K16. doi: 10.1029/2011JA016429
- 1045 Meng, C.-I., Lui, A. T. Y., Krimigis, S. M., Ismail, S., & Williams, D. J. (1981,  
1046 July). Spatial distribution of energetic particles in the distant magne-  
1047 totail. *Journal of Geophysical Research*, *86*, 5682-5700. doi: 10.1029/  
1048 JA086iA07p05682
- 1049 Otto, A. (2001, Mar). Geospace Environment Modeling (GEM) magnetic re-  
1050 connection challenge: MHD and Hall MHD-constant and current dependent  
1051 resistivity models. *Journal of Geophysical Research*, *106*(A3), 3751-3758. doi:  
1052 10.1029/1999JA001005
- 1053 Pontin, D. I. (2020, February). Magnetohydrodynamic reconnection, oxford re-  
1054 search encyclopedia of physics. Oxford University Press Online. doi: 110.1093/  
1055 acreate/9780190871994.013.5
- 1056 Pritchett, P. L. (2001, March). Geospace environment modeling magnetic recon-  
1057 nection challenge: Simulations with a full particle electromagnetic code. *Journal  
1058 of Geophysical Research*, *106*(A3), 3783-3798. doi: 10.1029/1999JA001006
- 1059 Ricci, P., Lapenta, G., & Brackbill, J. U. (2002, December). Gem reconnection  
1060 challenge: Implicit kinetic simulations with the physical mass ratio. *Geophysics  
1061 Research Letters*, *29*, 2088. doi: 10.1029/2002GL015314
- 1062 Shay, M. A., Drake, J. F., Rogers, B. N., & Denton, R. E. (2001). Alfvnic collision-  
1063 less magnetic reconnection and the hall term. *Journal of Geophysical Research:  
1064 Space Physics*, *106*(A3), 3759-3772. doi: 10.1029/1999JA001007
- 1065 Shay, M. A., Drake, J. F., & Swisdak, M. (2007, October). Two-scale struc-  
1066 ture of the electron dissipation region during collisionless magnetic re-  
1067 connection. *Physical Review Letters*, *99*(15), 155002. doi: 10.1103/  
1068 PhysRevLett.99.155002
- 1069 Shay, M. A., & Swisdak, M. (2004, October). Three-Species Collisionless Recon-  
1070 nection: Effect of  $\text{O}^+$  on Magnetotail Reconnection. *Physical Review Letters*,  
1071 *93*(17), 175001. doi: 10.1103/PhysRevLett.93.175001
- 1072 Speiser, T. W. (1965, September). Particle trajectories in model current sheets, 1,  
1073 analytical solutions. *Journal of Geophysical Research*, *70*, 4219-4226. doi: 10  
1074 .1029/JZ070i017p04219
- 1075 Tenfjord, P., Hesse, M., Norgren, C., Spinnangr, S. F., & Kolstø, H. (2019, June).  
1076 The impact of oxygen on the reconnection rate. *Geophysics Research Letters*,  
1077 *46*(12), 6195-6203. doi: 10.1029/2019GL082175
- 1078 Uzdensky, D. A., & Loureiro, N. F. (2016, March). Magnetic Reconnection Onset  
1079 via Disruption of a Forming Current Sheet by the Tearing Instability. *Physics  
1080 Review Letters*, *116*(10), 105003. doi: 10.1103/PhysRevLett.116.105003
- 1081 Wiltberger, M., Lotko, W., Lyon, J. G., Damiano, P., & Merkin, V. (2010, Oct).  
1082 Influence of cusp  $\text{O}^+$  outflow on magnetotail dynamics in a multifluid MHD  
1083 model of the magnetosphere. *Journal of Geophysical Research (Space Physics)*,  
1084 *115*(12), A00J05. doi: 10.1029/2010JA015579

- 1085 Winglee, R. M. (2004, Sep). Ion cyclotron and heavy ion effects on reconnection in a  
1086 global magnetotail. *Journal of Geophysical Research (Space Physics)*, 109(A9),  
1087 A09206. doi: 10.1029/2004JA010385
- 1088 Wygant, J. R., Cattell, C. A., Lysak, R., Song, Y., Dombek, J., McFadden, J., ...  
1089 Mouikis, C. (2005, September). Cluster observations of an intense normal  
1090 component of the electric field at a thin reconnecting current sheet in the tail  
1091 and its role in the shock-like acceleration of the ion fluid into the separatrix  
1092 region. *Journal of Geophysical Research (Space Physics)*, 110, A09206. doi:  
1093 10.1029/2004JA010708
- 1094 Zweibel, E. G., & Yamada, M. (2016, December). Perspectives on magnetic re-  
1095 connection. *Proceedings of the Royal Society of London Series A*, 472(2196),  
1096 20160479. doi: 10.1098/rspa.2016.0479

Figure 1.

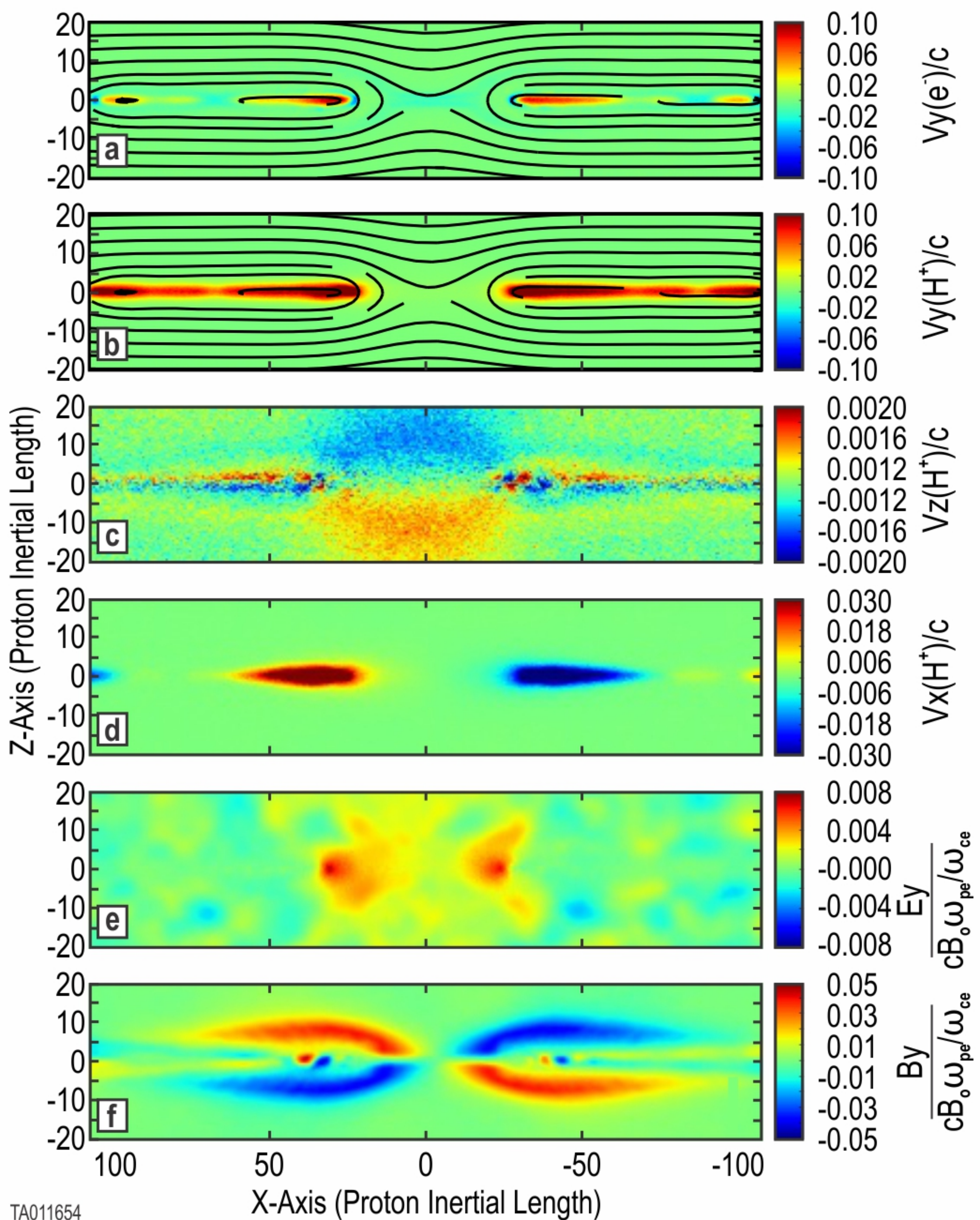


Figure 2.

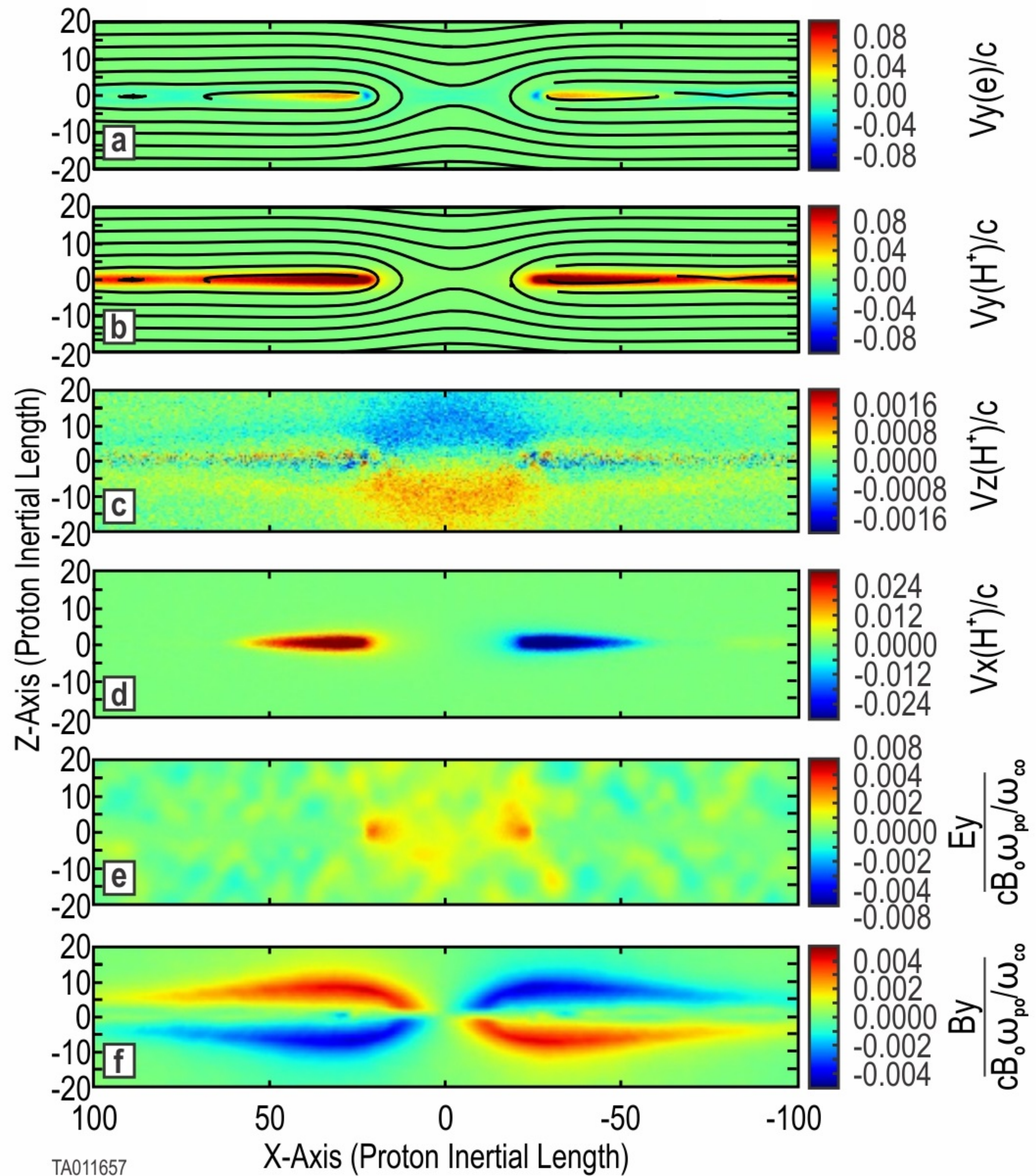
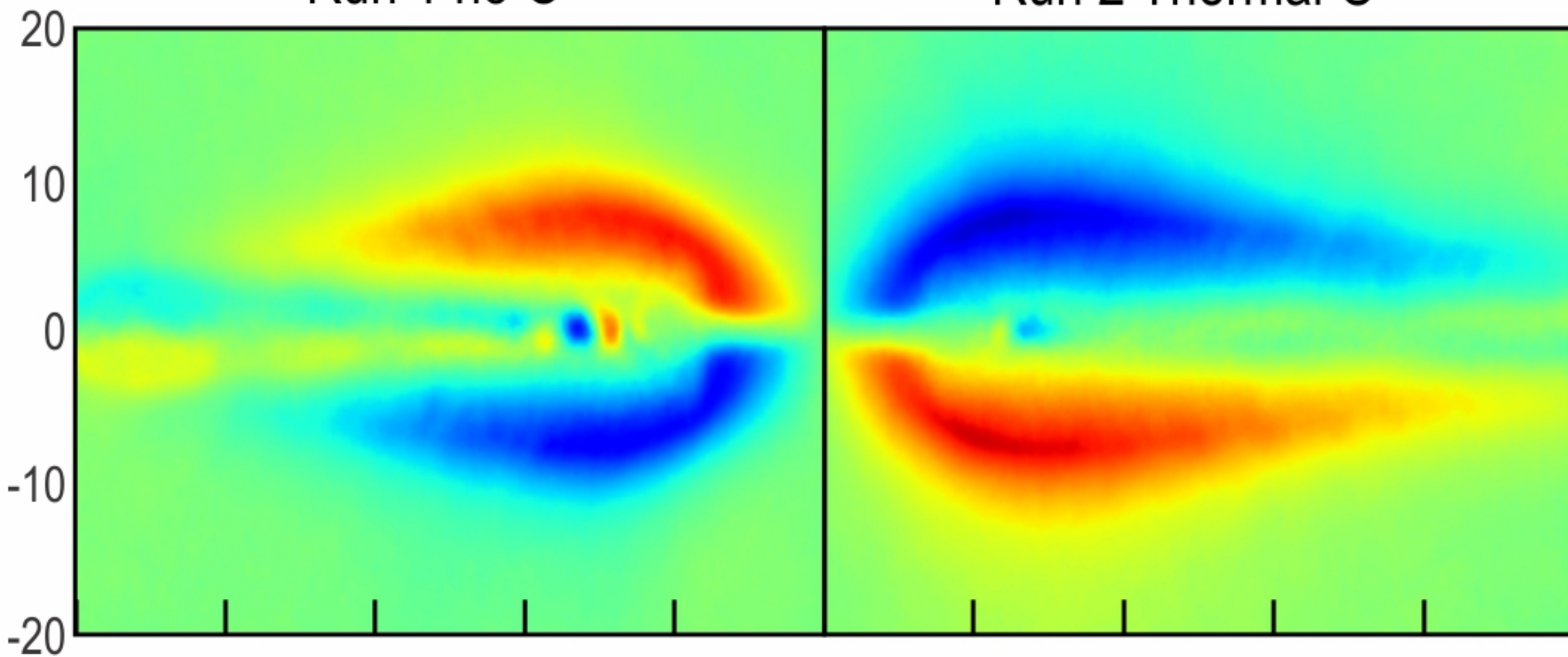
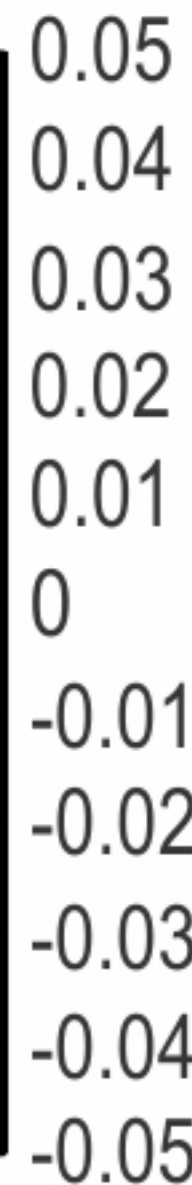


Figure 3.

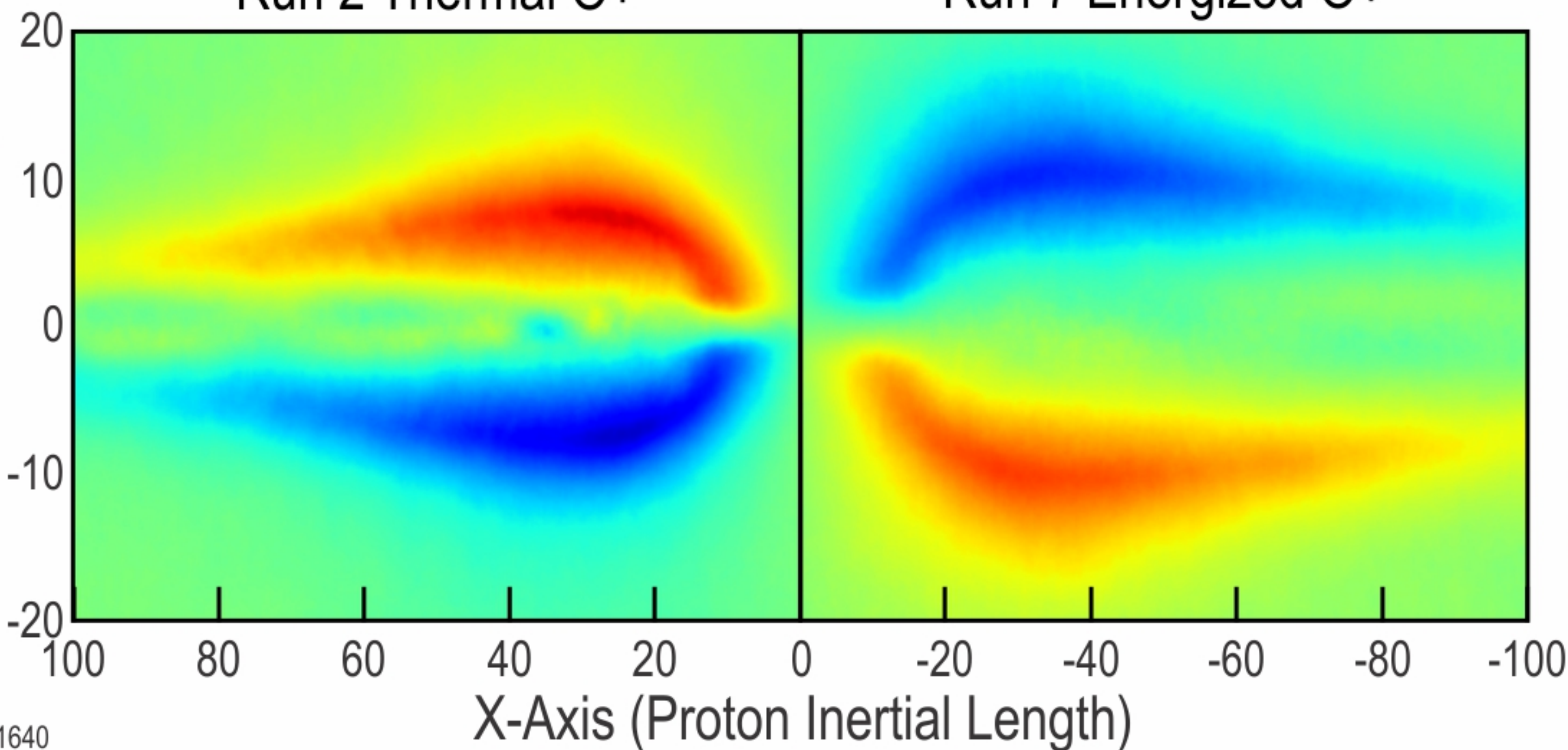
Run 1 no O+

Run 2 Thermal O+


 $B_y / (B_0 \omega_{pe} / \omega_{ce})$ 


Run 2 Thermal O+

Run 7 Energized O+


 $B_y / (B_0 \omega_{pe} / \omega_{ce})$ 


**Figure 4.**

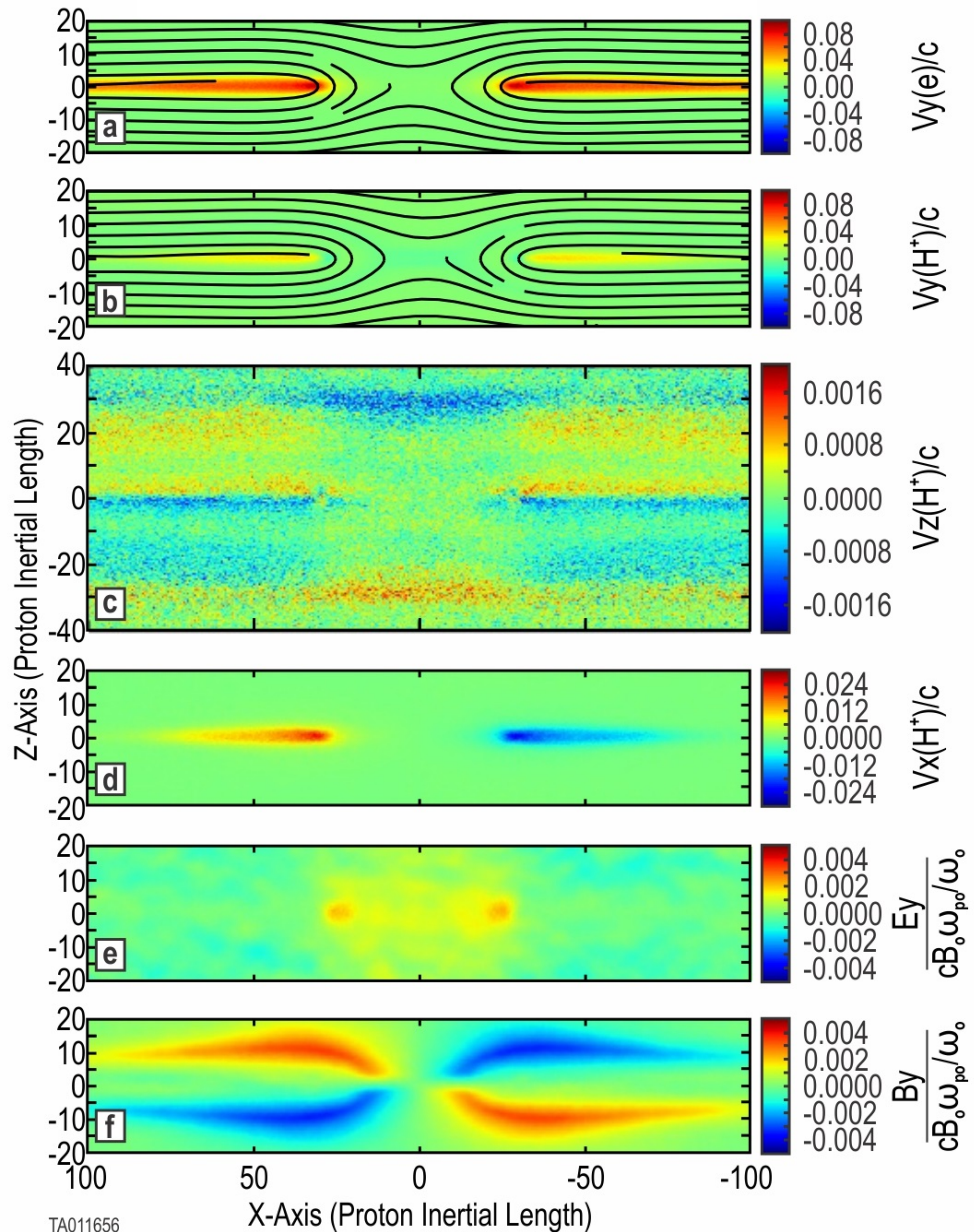


Figure 5.

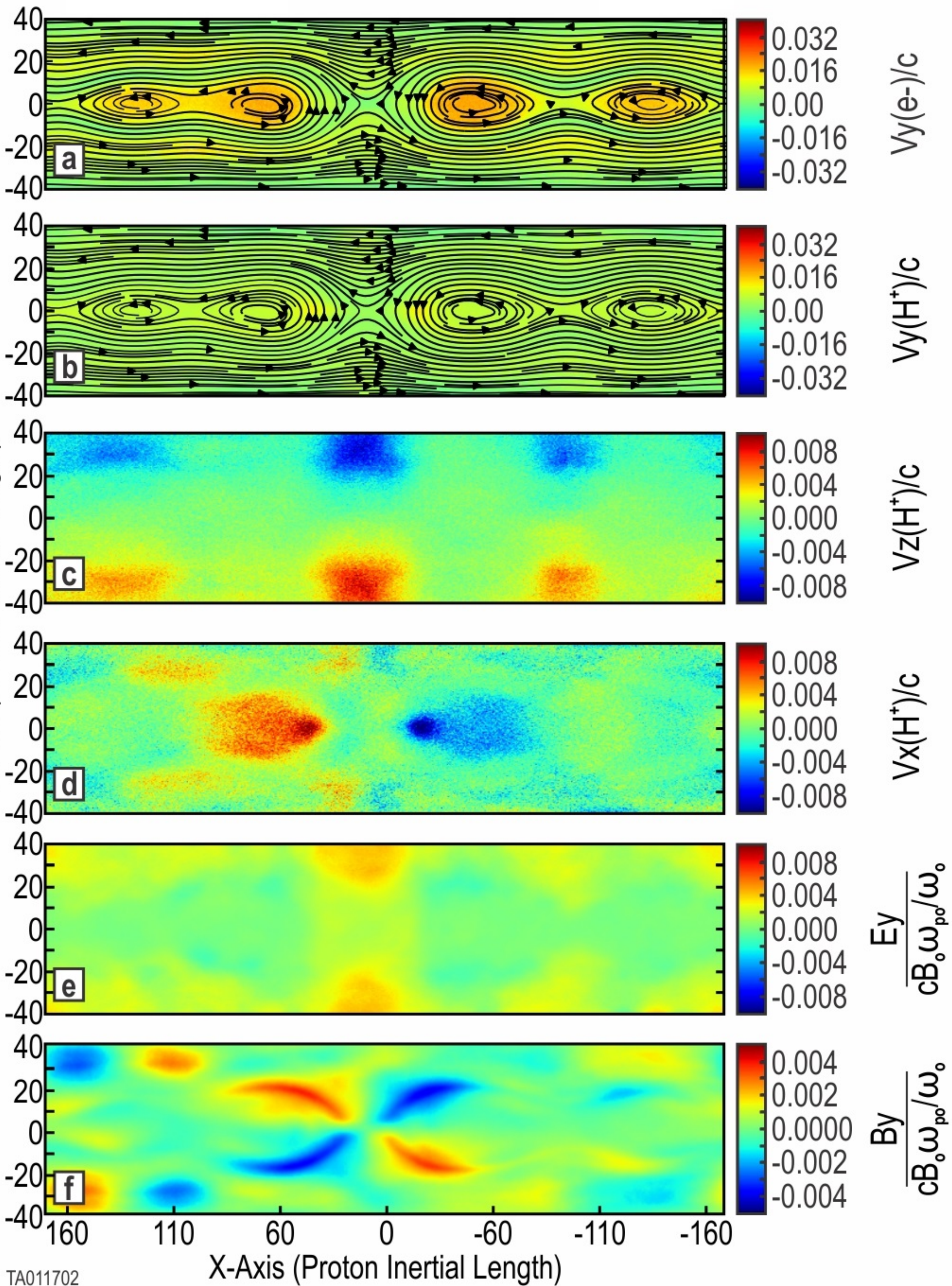


Figure 6.

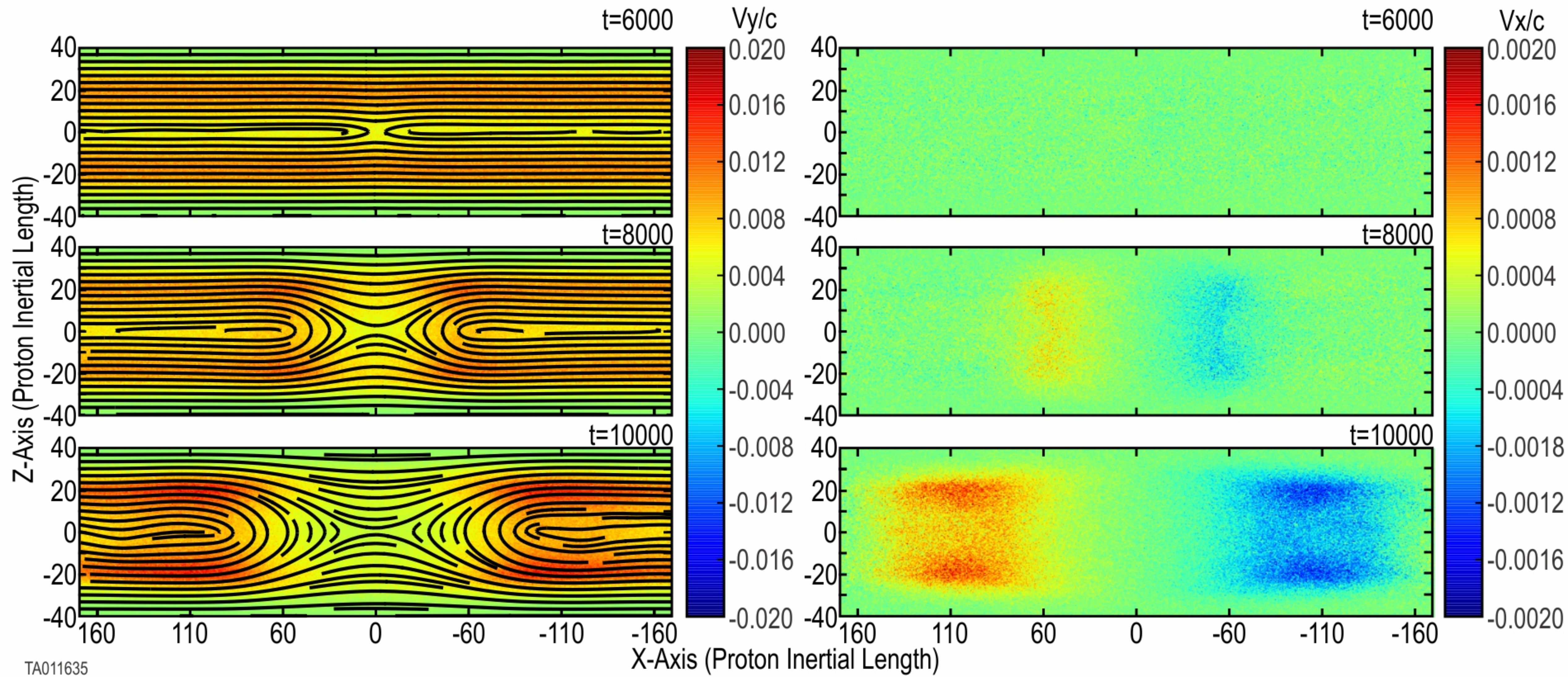


Figure 7.

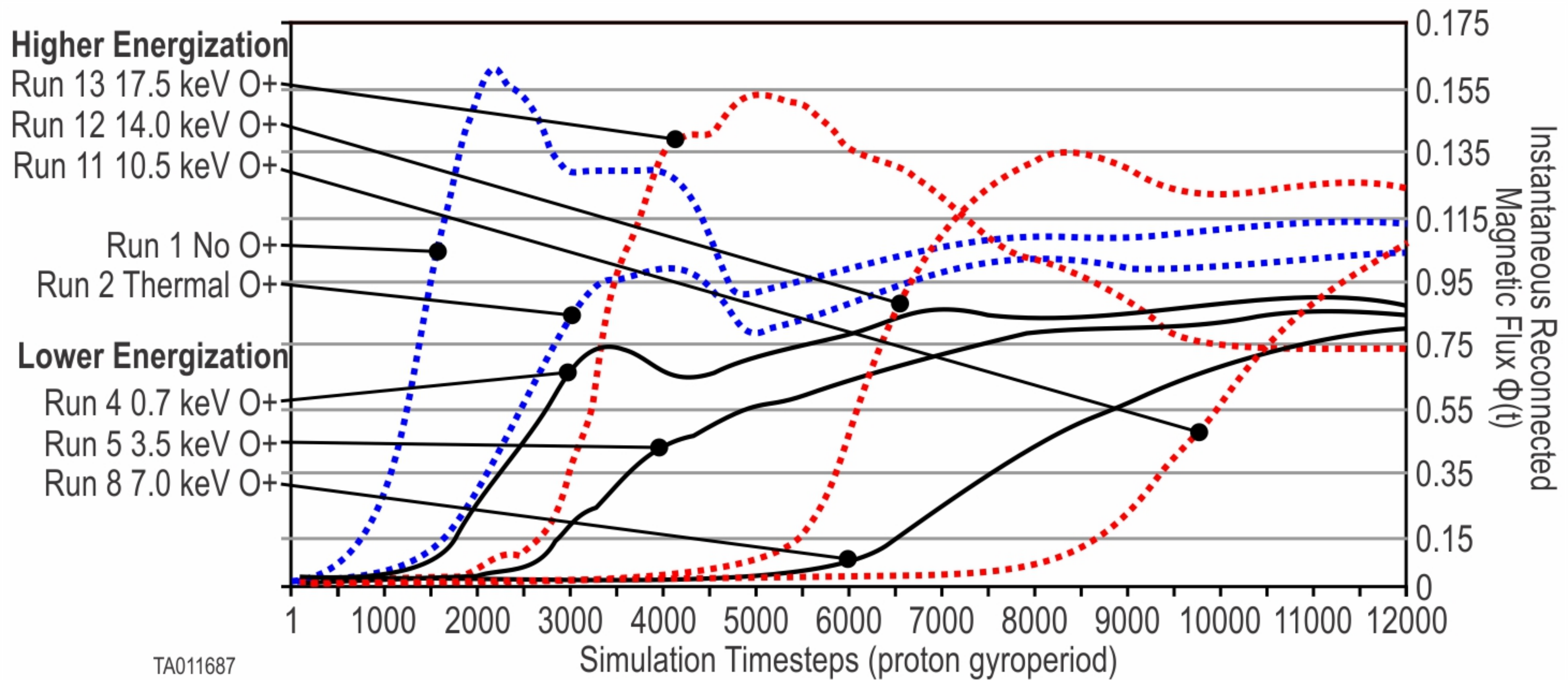


Figure 8.

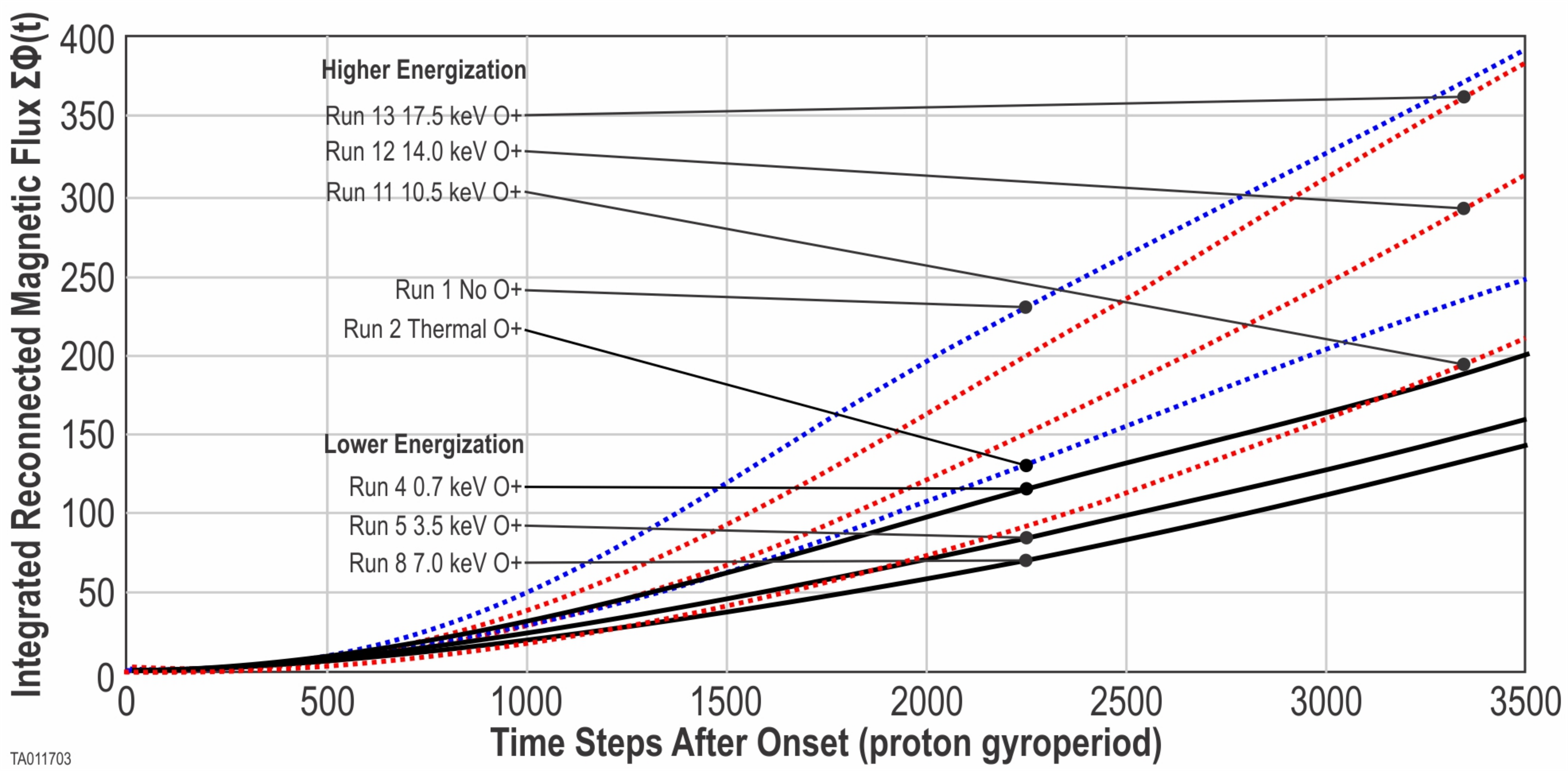


Figure 9.

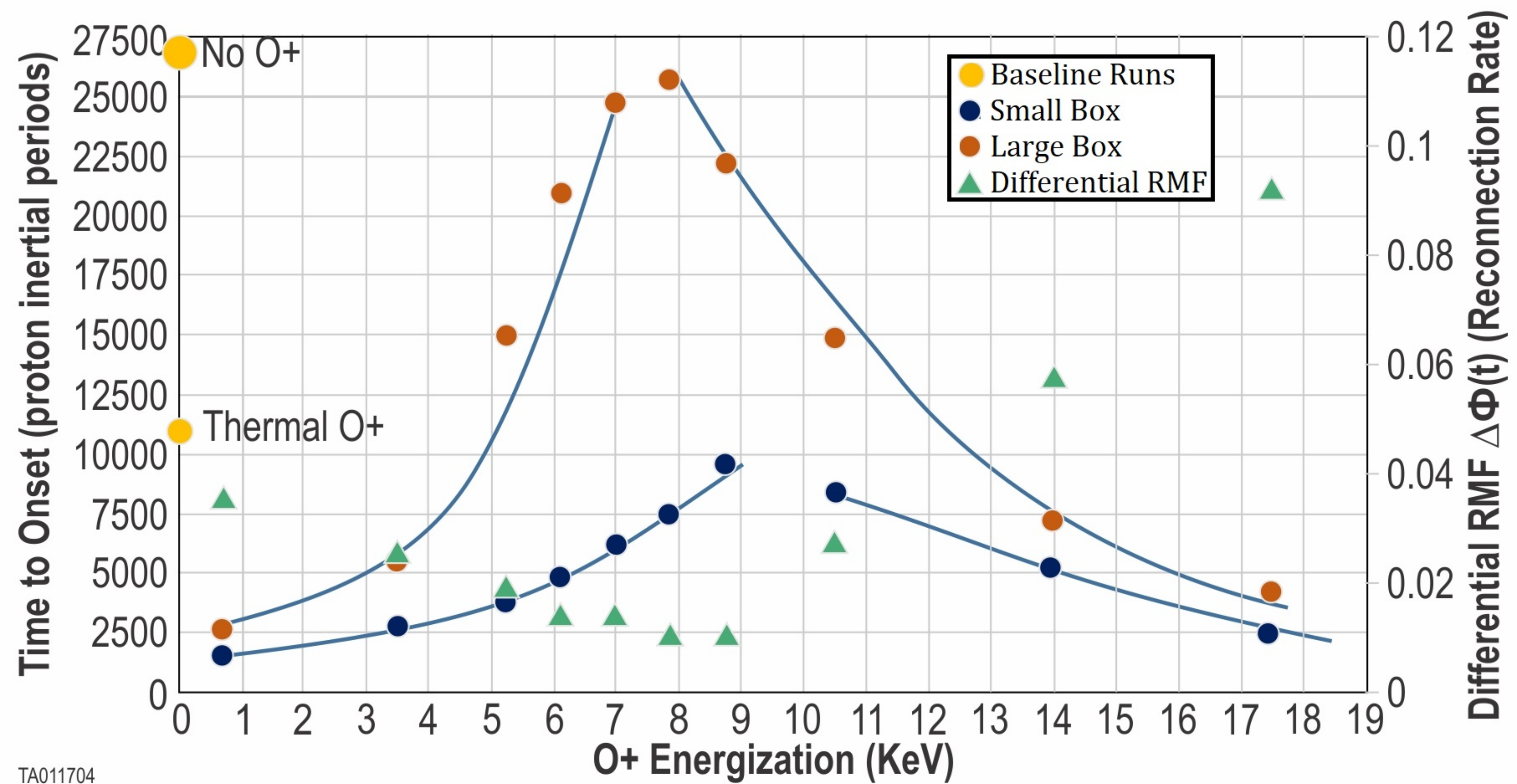


Figure 10.

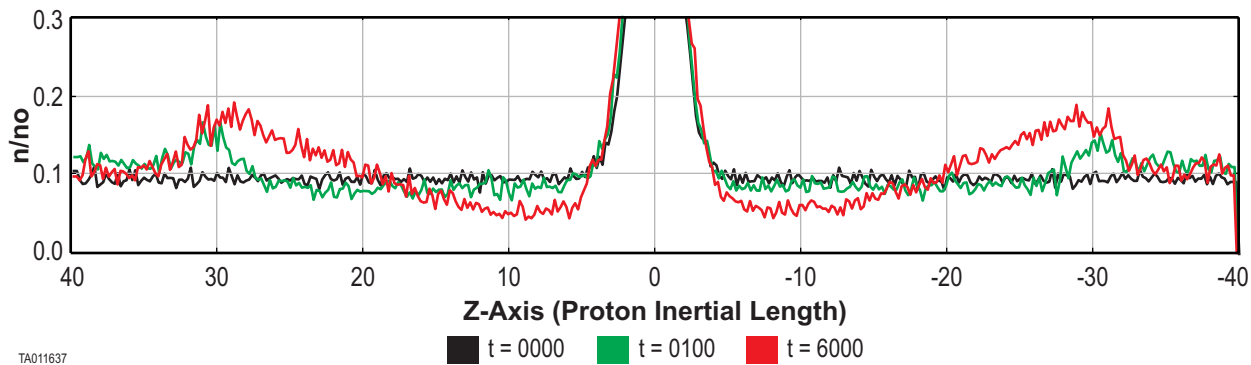


Figure 11.

